

# Multinuclear Solid-State Magnetic Resonance as a Sensitive Probe of Structural Changes upon the Occurrence of Halogen Bonding in Co-crystals

Cory M. Widdifield,<sup>[a, c]</sup> Gabriella Cavallo,<sup>[b]</sup> Glenn A. Facey,<sup>[a]</sup> Tullio Pilati,<sup>[b]</sup> Jingxiang Lin,<sup>[b]</sup> Pierangelo Metrangolo,<sup>\*, [b]</sup> Giuseppe Resnati,<sup>\*, [b]</sup> and David L. Bryce<sup>\*, [a]</sup>

**Abstract:** Although the understanding of intermolecular interactions, such as hydrogen bonding, is relatively well-developed, many additional weak interactions work both in tandem and competitively to stabilize a given crystal structure. Due to a wide array of potential applications, a substantial effort has been invested in understanding the halogen bond. Here, we explore the utility of multinuclear (<sup>13</sup>C, <sup>14/15</sup>N, <sup>19</sup>F, and <sup>127</sup>I) solid-state magnetic resonance experiments in characterizing the electronic and structural changes which take place upon the formation of five halogen-bonded co-crystalline product materials. Single-crystal X-ray diffraction (XRD) structures of three novel co-crystals which exhibit a 1:1 stoichiometry between decamethonium diiodide (i.e., [(CH<sub>3</sub>)<sub>3</sub>N<sup>+</sup>(CH<sub>2</sub>)<sub>10</sub>N<sup>+</sup>(CH<sub>3</sub>)<sub>3</sub>][2I<sup>-</sup>])

and different *para*-dihalogen-substituted benzene moieties (i.e., *p*-C<sub>6</sub>X<sub>2</sub>Y<sub>4</sub>, X=Br, I; Y=H, F) are presented. <sup>13</sup>C and <sup>15</sup>N NMR experiments carried out on these and related systems validate sample purity, but also serve as indirect probes of the formation of a halogen bond in the co-crystal complexes in the solid state. Long-range changes in the electronic environment, which manifest through changes in the electric field gradient (EFG) tensor, are quantitatively measured using <sup>14</sup>N NMR spectroscopy, with a systematic decrease in the <sup>14</sup>N quadrupolar coupling constant

(C<sub>Q</sub>) observed upon halogen bond formation. Attempts at <sup>127</sup>I solid-state NMR spectroscopy experiments are presented and variable-temperature <sup>19</sup>F NMR experiments are used to distinguish between dynamic and static disorder in selected product materials, which could not be conclusively established using solely XRD. Quantum chemical calculations using the gauge-including projector augmented-wave (GIPAW) or relativistic zeroth-order regular approximation (ZORA) density functional theory (DFT) approaches complement the experimental NMR measurements and provide theoretical corroboration for the changes in NMR parameters observed upon the formation of a halogen bond.

**Keywords:** co-crystallization • halogen bonds • noncovalent interactions • NMR spectroscopy • X-ray diffraction

## Introduction

A variety of noncovalent and generally weakly stabilizing intra- and intermolecular interactions are known to assist in the organization of supramolecular systems in the solid state.<sup>[1]</sup> Of these weak interactions, hydrogen bonding<sup>[2–4]</sup> is

perhaps the most well-documented, finding many applications in crystal engineering,<sup>[5]</sup> materials design,<sup>[6]</sup> and biochemical/biological processes.<sup>[7]</sup> In addition to hydrogen bonding, several additional interactions are also believed to be significant in many of the same applications (e.g., anion–π,<sup>[8–10]</sup> cation–π,<sup>[11,12]</sup> π–π,<sup>[13]</sup> lone pair–π,<sup>[14,15]</sup> CH–π,<sup>[16–18]</sup> metallophilic<sup>[19–21]</sup>), and it is understood that these weak interactions can operate in cooperative,<sup>[22–24]</sup> competitive,<sup>[25,26]</sup> or independent<sup>[27]</sup> fashions. Halogen bonding is one member of this group of additional interactions. Halogen bonding is said to occur between a halogen atom, which acts as an electrophile, and some suitable electron donating moiety (examples of halogen bond acceptors include the oxygen atoms in 1,4-dioxane, nitrogen atoms in ammonia, selenium atoms in tetrahydroselenophene, and halide anions).<sup>[1,28–31]</sup> Although donor–acceptor interactions which involve a halogen atom are not new,<sup>[32,33]</sup> interest in using halogen bonding as a tool in supramolecular chemistry, anion binding, and functional materials design is a relatively recent phenomenon.<sup>[34–36]</sup> Although it is beyond the scope of the current study to provide a comprehensive review of the literature, a number of recent reviews on halogen bonding are recommended.<sup>[29,30,34,37–40]</sup>

[a] Dr. C. M. Widdifield, Dr. G. A. Facey, Prof. D. L. Bryce  
Department of Chemistry and Centre for Catalysis Research and Innovation, University of Ottawa, 10 Marie Curie Pvt.  
Ottawa, Ontario (Canada)  
E-mail: dbryce@uottawa.ca

[b] Prof. G. Cavallo, Dr. T. Pilati, J. Lin, Prof. P. Metrangolo, Prof. G. Resnati  
NFMLab–D.C.M.I.C. “Giulio Natta”, Politecnico di Milano  
Via L. Mancinelli 7, 20131 Milano (Italy)  
E-mail: pierangelo.metrangolo@polimi.it  
giuseppe.resnati@polimi.it

[c] Dr. C. M. Widdifield  
Present Address: Centre de RMN à Très Hauts Champs  
Université de Lyon (CNRS/ENS Lyon/UCB Lyon 1)  
69100 Villeurbanne (France)

Supporting information for this article is available on the WWW under <http://dx.doi.org/10.1002/chem.201300809>.

Somewhat recently, it was demonstrated that bis(trimethylammonium)alkane diiodides could dynamically and reversibly encapsulate diiodoperfluoroalkanes, and that the process was largely driven by intermolecular halogen bonding between the iodide anions present in the host material and the terminal iodine atoms of the guest.<sup>[41]</sup> Based on these previous accounts, it appears that bis(trimethylammonium)alkane diiodide host materials could be used to dynamically create many new supramolecular environments, which are organized in part due to the halogen bonding between the iodide anions of the alkane diiodide and halogen atoms (including Cl, Br, I) of properly selected guest molecules.

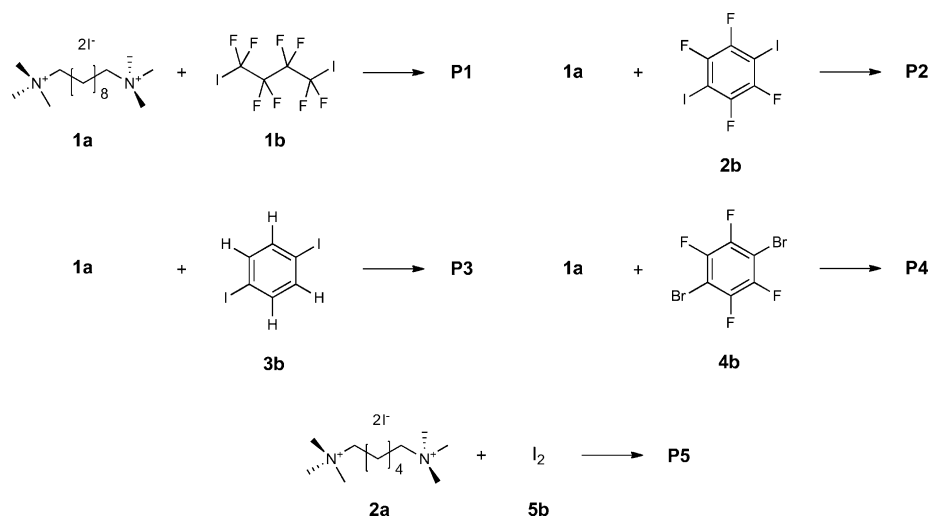
Simultaneously, there has been substantial recent development in the field of solid-state NMR (SSNMR) of the quadrupolar halogen nuclei (i.e., <sup>35/37</sup>Cl, <sup>79/81</sup>Br, <sup>127</sup>I),<sup>[42–46]</sup> including the first direct SSNMR observations of covalently bound chlorine atoms in organic compounds.<sup>[47]</sup> Recent preliminary accounts of halogen SSNMR measurements of the halide anions in a variety of haloanilinium halide systems demonstrated a weak correlation between the strength of a halogen bond and several SSNMR observables, including the isotropic chemical shift value of the halide anion.<sup>[48]</sup> At the same time, it was also noted that further work was required in order to understand the individual effects of halogen bonding and hydrogen bonding on the resulting SSNMR spectra of the halide anions, as it is often the case that these interactions will be present simultaneously. In addition to these recent advances in halogen SSNMR, <sup>14</sup>N SSNMR methods have also been enhanced over the course of the last few years,<sup>[49–52]</sup> and it appears that the direct observation of even low-symmetry nitrogen environments is feasible, so long as the correct experimental tools are both available (i.e., large magnetic fields, *B*<sub>0</sub>) and relevant (i.e., long *T*<sub>2</sub> values for data acquisition) to the system under study.

In the present study, we outline the synthesis, structural description, and multinuclear solid-state magnetic resonance characterization of a series of halogen-bonded co-crystals involving bis(trimethylammonium)alkane diiodides. Although <sup>13</sup>C and <sup>15</sup>N SSNMR experiments largely serve to confirm the purity of most of the materials studied, drastic changes in the <sup>14</sup>N quadrupolar coupling constant (*C*<sub>Q</sub>) upon formation of the supramolecular systems are consistently observed. In addition, we assess whether the <sup>13</sup>C isotropic chemical shift value of a carbon atom directly attached to a halogen atom may serve as a useful indirect probe of the occurrence of halogen bonding. Where possible, <sup>127</sup>I SSNMR

experiments are attempted, but high-quality spectral data are not always possible to acquire, due to the very large quadrupolar interaction (QI) for the iodine-127 nuclide. This study also presents a unique application of solid-state <sup>14</sup>N NMR experiments to probe the formation of supramolecular systems. To obtain additional insights, the experimental <sup>13</sup>C, <sup>14</sup>N, and <sup>127</sup>I SSNMR data are complemented with quantum chemical computations, which employ either the gauge-including projector augmented-wave (GIPAW) density functional theory (DFT) method,<sup>[53–57]</sup> or the zeroth-order regular approximation (ZORA)<sup>[58–61]</sup> DFT formalism.

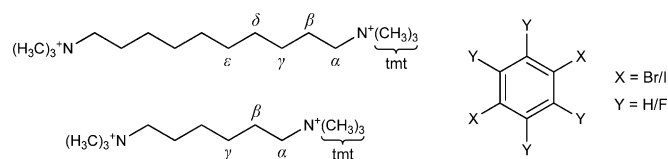
## Results and Discussion

The component building blocks, co-crystallization reactions performed, as well as the shorthand notations used in the subsequent discussion, are depicted in Scheme 1. The label-



Scheme 1. Labeling notation and co-crystallizations performed as part of this study.

ing scheme for reporting <sup>13</sup>C chemical shifts is in Scheme 2. In all, five halogen-bonded co-crystals were studied using NMR spectroscopy (i.e., **P1–P5**), as well as many of the starting materials (i.e., **1a**, **2a**, **2b**, **3b**, **4b**). Please note that the reagent materials **1a** and **2a** actually exist as dihydrates (i.e., SSNMR experiments were performed upon **1a·2H<sub>2</sub>O** and **2a·2H<sub>2</sub>O**) although the water molecules neither participate in the generation of, nor are they included within, the product materials.



Scheme 2. Labeling scheme used for molecular fragments in this study (see also Table 1), where tmt = trimethyl.

**Single crystal X-ray diffraction analysis:** Single crystal X-ray diffraction analysis of **P2**, **P3**, and **P4** revealed that all of the complexes crystallize in the same space group,  $C2m$ , as previously found also for **P1**<sup>[41]</sup> and **P5**,<sup>[62]</sup> and confirmed the 1:1 ratio between the decamethonium iodide salt and the halogen bond donor. The diiodo- and dibromobenzene modules act as bidentate ligands, giving rise to linear trimeric superanions upon interaction with two iodides, with  $X\cdots I^-$  ( $X=I, Br$ ) distances of 3.5308(13), 3.5222(4), and 3.6318(14) Å and  $C-X\cdots I^-$  angles of 174.42(2), 179.96(10), and 173.52(3)°, respectively, for **P2**, **P3**, and **P4**. Both the cation and the superanion lie on crystallographic  $2m$  positions, as found in **P1**<sup>[41]</sup> and **P5**.<sup>[62]</sup> However, notwithstanding these similarities, all the novel structures analyzed in this study are quite different from those previously reported.

Although in **P1** and **P5** the superanions, trapped in a parallelepiped-shaped cavity, are completely isolated and hence do not interact with one another, the superanions in **P3** are linked together by pairs of  $I\cdots H$  centrosymmetric contacts (3.16 Å), forming an ordered column. Other contacts slightly shorter than the sum of van der Waals radii of the involved atoms are also present, for example, between the iodine atoms on the 1,4-diiodobenzene module and the  $\alpha$ -methylene H atoms on the cation (four equivalent  $H\cdots I$  contacts of 3.13 Å, involving four different cations), and the iodide anions and the methyl H atoms (four equivalent  $H\cdots I^-$  contacts of 3.16 Å, involving two different cations; Figure 1).

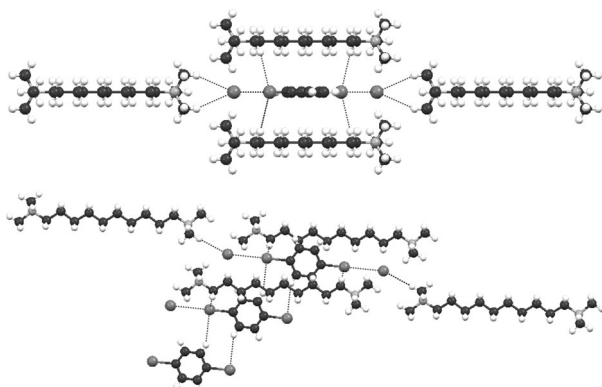


Figure 1. A cluster of cations and superanions of **P3**. Top: projection down  $c$ ; bottom: view along  $b$ . The short interactions  $H\cdots I$  and  $H\cdots I^-$  are highlighted using dotted lines.

**P2** and **P4** have structures quite different from **P3**. In **P2**, the cation is parallel to  $a$ , whereas it is parallel to the (102) plane in **P4**; nevertheless, these two co-crystals are isomorphous. This is because of the different reduced cell. In fact, the application of a proper cell transformation for **P4** makes evident the isomorphous relationship between the two co-crystals. Consequently, most of the discussion of one structure also applies to the second one. Both **P2** and **P4** gave good quality single crystals that, unfortunately, were poorly diffracting, showing anisotropic spots and diffuse strikes typical of disorder. We tried to collect data at low temperature

in order to avoid disorder, but either crystal cracking or a phase transition occurred upon cooling below room temperature, with consequent worsening of the intensity data. However, for both the co-crystals we collected data to a sufficient resolution for structure refinement. Both in **P2** and **P4** the dihalotetrafluorobenzene module lies on a crystallographic  $2m$  position. It is disordered, half lying on the mirror plane (hereinafter we will call this moiety BnzP). By rotation of 90° around the  $I\cdots I$  axis, that is, the one of minimum inertia, we obtain the second half of this molecule (hereinafter BnzO). We tried to refine the complementary population factors for the two orthogonal models, but they converged at about 0.5 so we assumed exactly this value, also imposed by our interpretation of the disorder. As for the cation, its refinement with an ordered model gave very poor results, partly because of very unusual C–C distances, due to the large anisotropic displacement parameters (ADPs) for the cited C atoms. We decided to impose some restraints on the geometry of the cation, but the anomalies on its ADPs did not change. The structural disorder found for **P2** and **P4** requires a rationalization. It is clearly localized around the plane  $x=0.0$  (and 0.5), whereas around the

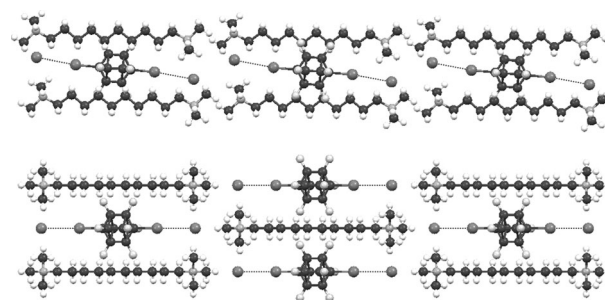


Figure 2. Packing of **P2** viewed along  $b$  (top) and  $c$  (bottom); atoms in ADPs style. Dotted lines represent short intermolecular contacts; some of these are physically impossible and limit the mutual presence of various conformers of cations and superanions.

plane  $x=0.25$  (and 0.75) all is ordered (Figure 2). Since there are no strong interactions between adjacent disordered layers, the disorder in one layer does not influence the disorder in any other layers. Thus, we can limit our structural analysis to the portion between the plane with  $x=0.25$  and the one with  $x=0.75$ . We noted that the BnzP moiety of diiodotetrafluorobenzene is incompatible with itself since there are absurd contacts with the nearest symmetry related molecule, as for example, the distance  $F2A\cdots F1A(x,y,1+z)=1.411$  Å. The only possible explanation is that molecules BnzP and BnzO alternate systematically in the direction (001). To rationalize the disorder we prepared Figure 3, assuming a cell with doubled  $c$ , duplicating all the molecules in the cell to reproduce the same plot of the real structure, thus eliminating, along  $c$ , alternatively a BnzO and a BnzP moiety.

The result is obviously much more “clean”, but some very short  $H\cdots F$  contacts (about 2.0 Å) are still present. We can

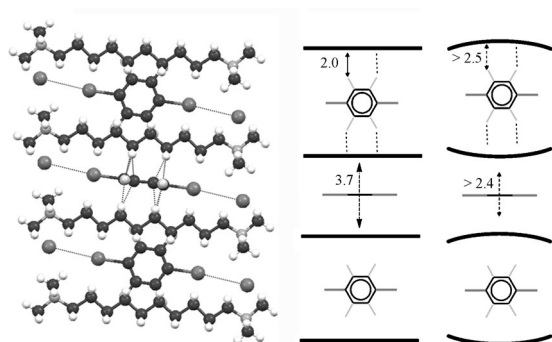


Figure 3. Left: view along *b* of a **P2** layer after alternating elimination of a BnzO and a BnzP moiety as explained in the main text; dotted lines represent F...H and F...C short contacts. Right: a sketched representation of two possible conformations for the cation chains: a linear conformation and a bent conformation. Upon deformation of the cationic chains, the critical F...H distances between BnzP and the cations, and the large void between the central cation chains, change significantly. Increasing F...H distances to acceptable values would be compatible with the minimum distance between the central cations. Experimental data indicating the substantial correctness of the “bent” model are the N...N intramolecular distances: 14.023(6), 13.430(12), and 13.315(11) Å, respectively, for **P3**, **P2**, and **P4**; such a contraction of the cation may be explained only in two ways: an alternance of enlarged and reduced C–C–C angles along the chain N–C<sub>10</sub>–N or by single or superimposed ttgttgtt and tttgttgtt conformations rather than the all-*trans* one. We propose that the second hypothesis is the most probable, but the irremediable low data/parameters ratio and the low quality of the X-ray diffraction data made it impossible to refine such a model.

explain these anomalous contacts by taking into account the very large ADPs of the central part of the cations, consistent with a superimposition of two conformations of the (CH<sub>3</sub>)<sub>3</sub>N<sup>+</sup>(CH<sub>2</sub>)<sub>10</sub>N<sup>+</sup>(CH<sub>3</sub>)<sub>3</sub> chains, and “bent” in opposite directions with respect to *c*. Figure 3 reports on the left the “real” cation conformation viewed along *b*, and on the right a sketch representing two possible conformations suggested for the cation: a linear conformation showing the critical F...H distances between the BnzP and the cation and the large void between the two central cation chains and a possible cation bent conformation, with the consequent significant modification of these critical distances. Since there is no real interference between adjacent layers, the plot on the right is valid also if translated along *c*, so that the “mean” structure comes to coincide with the “real” one, with BnzO and BznP and two superimposed chains “bent” on opposite directions. From the crystallographic point of view our understanding of the structure seems reasonable. As it is impossible to collect adequate data at a lower temperature, there is no possibility to understand solely from these X-ray studies if the disorder is static or dynamic. NMR results, however, suggest static disorder (vide infra).

**Solid-state <sup>13</sup>C and <sup>15</sup>N NMR spectroscopy:** As part of the characterization process, many of the starting materials, as well as all of the product materi-

als, were subjected to <sup>13</sup>C and <sup>15</sup>N solid-state NMR experiments with sensitivity enhancement being provided by cross-polarization (CP) from the abundant <sup>1</sup>H nuclei, if possible. Certain materials did not contain <sup>1</sup>H nuclei (i.e., **2b** and **4b**), and therefore direct detection <sup>13</sup>C NMR experiments were performed. The observed isotropic chemical shifts for the carbon and nitrogen nuclei are given in Table 1 and Table 2.

Although all <sup>13</sup>C NMR and most <sup>15</sup>N NMR experiments were performed under magic-angle spinning (MAS) conditions, in order to establish the significance of nitrogen chemical shift anisotropy (CSA), both in the starting materials and upon formation of the supramolecular systems, <sup>15</sup>N ramped-amplitude cross-polarization (RAMP-CP)/static experiments were also conducted on some of the samples (Supporting Information, Figures S1 and S2). It is not terribly surprising that the nitrogen CS tensor span (Ω) values for several of the systems are rather small (Ω < 20 ppm). These observations are consistent with the relatively high nitrogen site symmetry in these materials, as established using X-ray diffraction data (vide supra). As well, a change in the nitrogen CSA upon complex formation could not be established within measurement errors (see Supporting Information, Figure S1). At the same time, it is pointed out that a slight systematic paramagnetic shift (i.e., deshielding) in the δ<sub>iso</sub>(<sup>15</sup>N) value upon complex formation was measured (Figure 4 and Figure 5) and for all product complexes, there is a significant reduction in the <sup>15</sup>N NMR line width relative to the appropriate starting material (also see Figure 4 for selected examples of the <sup>15</sup>N NMR signal line widths at half-height (Δν<sub>1/2</sub>)). For the complexes based on the decamethonium cation (Figure 4), the average shift in δ<sub>iso</sub>(<sup>15</sup>N) upon product complex formation is +1.92 ppm (standard deviation = 0.24 ppm). In the case of the systems based upon the hexamethonium cation (Figure 5), the shift upon formation of the supramolecular complex was more modest for the only pair featured in the present study (i.e., Δδ<sub>iso</sub>(<sup>15</sup>N) = +

Table 1. Experimental <sup>13</sup>C and <sup>15</sup>N SSNMR data for systems herein: alkyl cations.<sup>[a]</sup>

Compound	δ <sub>iso</sub> ( <sup>13</sup> C, α) [ppm]	δ <sub>iso</sub> ( <sup>13</sup> C, β) [ppm]	δ <sub>iso</sub> ( <sup>13</sup> C, γ) [ppm]	δ <sub>iso</sub> ( <sup>13</sup> C, δ/ε) [ppm]	δ <sub>iso</sub> ( <sup>13</sup> C, tmt) [ppm]	δ <sub>iso</sub> ( <sup>15</sup> N) [ppm]
<b>1a-2H<sub>2</sub>O</b>	67.15	26.17	28.05	31.64/31.97	52.96	–328.70
<b>2a-2H<sub>2</sub>O</b>	67.18	26.35	27.64	–	56.15	–326.86
<b>P1</b>	66.81	25.01	28.31	31.15	55.48	–326.72
<b>P2</b>	66.27	24.78/ 24.46	28.09	32.66 <sup>[b]</sup>	55.77	–326.58
<b>P3</b>	68.38	24.88	27.16	32.14/33.02	55.76	–327.14
<b>P4</b>	65.56/ 65.06	23.90/ 24.37	26.80	33.17/ 32.36 <sup>[b]</sup>	55.86/55.39	–326.70
<b>P5</b>	65.37	24.54	28.56	–	56.37	–325.94

[a] Errors in the chemical shift values ranged from 0.06–0.21 ppm for <sup>13</sup>C and 0.05–0.14 ppm for <sup>15</sup>N, and correspond to half the line width at 90% of the full peak intensity. Labeling scheme and compound naming conventions used are provided in Scheme 2. For the full <sup>13</sup>C SSNMR spectra, please see the Supporting Information, Figure S3–S4. All <sup>13</sup>C chemical shifts are with respect to neat tetramethylsilane (TMS) at 0 ppm, whereas all <sup>15</sup>N chemical shifts are with respect to neat nitromethane at 0 ppm, as detailed in the Experimental Section. [b] Additional peaks were found at about 30 ppm, and are thought to be due to δ/ε carbons experiencing C–H...F interactions, as detailed in the main text.

Table 2. Experimental  $^{13}\text{C}$  SSNMR data for systems herein:  $p\text{-C}_6\text{X}_2\text{Y}_4$  moieties.<sup>[a]</sup>

Compound	$\delta_{\text{iso}}(^{13}\text{C}, \text{C}(\text{X}=\text{Br/I}))$ [ppm]	$\delta_{\text{iso}}(^{13}\text{C}, \text{C}(\text{Y}=\text{H/F}))$ [ppm]
<b>2b</b>	77.2(0.8)	147.9/146.5
<b>3b</b>	ca. 99–100	141.3(0.3)/139.1(0.3)
<b>4b</b>	100.5(1.0)	146.5(1.5)
<b>P2</b>	ca. 82.5	ca. 146.7
<b>P3</b>	ca. 105–106	140.2(0.3)
<b>P4</b>	102.96(0.10)	144.41(0.16)/146.40(0.21)

[a] Where possible, errors in the chemical shift values correspond to half the line width at 90% of the full peak intensity. Labeling scheme and compound naming conventions used are provided in Scheme 2. For the full  $^{13}\text{C}$  SSNMR spectra, please see the Supporting Information, Figure S4–S5. All  $^{13}\text{C}$  chemical shifts are with respect to neat TMS at 0 ppm.

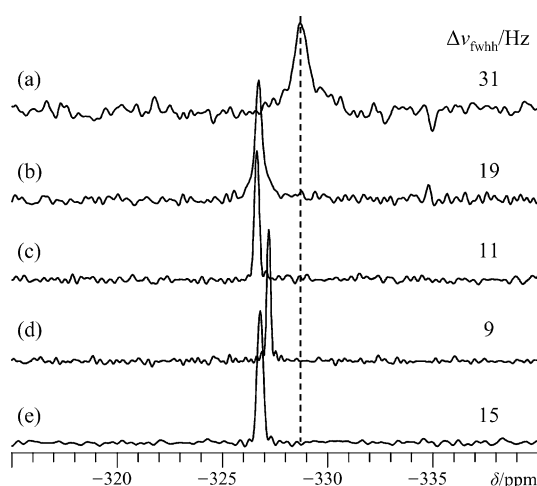


Figure 4. Experimental  $^{15}\text{N}\{^1\text{H}\}$  RAMP-CP/MAS NMR spectra of: a) **1a-2H<sub>2</sub>O**, b) **P1**, c) **P2**, d) **P3**, and e) **P4**. The spectra in (a), (b), and (c) were acquired at  $B_0=11.75$  T, whereas the spectra in (c) and (d) were acquired at  $B_0=9.4$  T. All spectra were acquired at  $T=285$  K, except for (e), which was acquired at room temperature. The dashed line highlights the systematic paramagnetic shift, which occurs upon formation of the product materials.

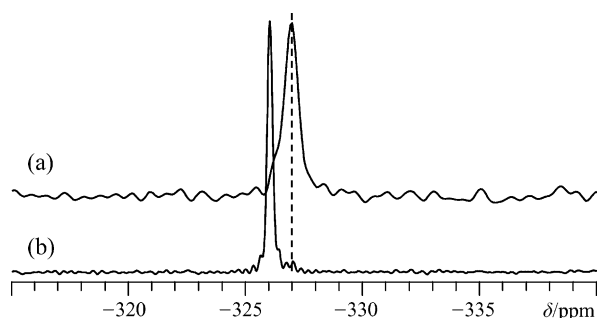


Figure 5. Experimental  $^{15}\text{N}\{^1\text{H}\}$  RAMP-CP/MAS NMR spectra of: a) **2a-2H<sub>2</sub>O**, and b) **P5**. All spectra were acquired at  $B_0=9.4$  T and  $T=293$  K. The dashed line highlights the paramagnetic shift, which occurs upon formation of the product material.

0.92 ppm), but it remains in the paramagnetic direction. The direction of this shift upon complex formation is opposite to what was observed for heteroatom containing hydrocarbons (such as quinuclidine) using liquid-state  $^{14}\text{N}$  data previously,<sup>[63a]</sup> however, it must be noted that the present class of

compounds is rather different as compared to the prior studies, as the nitrogen atoms in **P1–P5** are not direct participants in the halogen bond. To verify that these slight and positive changes in the nitrogen chemical shifts upon product formation are reasonable, GIPAW DFT computations were performed upon selected systems (**1a-2H<sub>2</sub>O**, **P3**, and **P5**), the results of which are briefly summarized in Table 3,

Table 3. GIPAW DFT-computed nitrogen and iodine NMR tensor parameters.<sup>[a]</sup>

Compound	Nucleus	$ C_Q(\text{X}) $ <sup>[b]</sup> [MHz]	$\eta_Q$	$\sigma_{\text{iso}}$ [ppm]	$\Omega$ [ppm]	$\delta_{\text{iso}}$ <sup>[c]</sup> [ppm]
<b>1a-2H<sub>2</sub>O</b>	$^{14/15}\text{N}$	0.126	0.402	168.95	17.37	–
	$^{127}\text{I}$	82.2	0.963	4855.71	175.52	181.79
<b>P3</b>	$^{14/15}\text{N}$	0.092	0.833	166.60	15.52	–
	$^{127}\text{I}^{[d]}$	174.6	0.257	4612.97	479.46	425.76
	$^{127}\text{I}^{[e]}$	1778.8	0.106	3382.40	2439.45	1662.56
<b>P5</b>	$^{14/15}\text{N}$	0.112	0.715	163.89	18.10	–
	$^{127}\text{I}^{[d]}$	418.6	0.179	4105.24	1265.07	936.06
	$^{127}\text{I}^{[e]}$	1936.8	0.064	3612.74	2706.24	1431.06

[a] Computational details may be found in the Supporting Information, Tables S7–S10. Prior to all NMR tensor parameter calculations, the hydrogen positions were subjected to a geometry optimization. Parameter definitions are as follows:  $C_Q = eQV_{33}/h$ ;  $\eta_Q = (V_{11} - V_{22})/V_{33}$ , where  $|V_{11}| \leq |V_{22}| \leq |V_{33}|$ ;  $\sigma_{\text{iso}} = (\sigma_{11} + \sigma_{22} + \sigma_{33})/3$ ;  $\Omega = \sigma_{33} - \sigma_{11}$ ;  $\kappa = 3(\sigma_{\text{iso}} - \sigma_{22})/\Omega$ , where  $\sigma_{11} \leq \sigma_{22} \leq \sigma_{33}$ ;  $\delta_{\text{iso}} = (\delta_{11} + \delta_{22} + \delta_{33})/3$ . [b] Although  $C_Q$  may take any real value,  $|C_Q|$  is measured using conventional SSNMR experiments. [c] Calculated iodine magnetic shielding values were converted into chemical shifts using the procedure outlined by Widdifield and Bryce,<sup>[64]</sup> and further described in the footnotes to Table S9 in the Supporting Information. [d] Values in this row correspond to the iodide anion. [e] Values in this row correspond to the iodine atom.

and more fully disclosed in the Supporting Information, Tables S7–S10. These three systems were chosen as they possess known crystal structures and there is no evidence of any significant structural disorder. Although the structural changes upon product formation about the nitrogen atoms are very modest (for example, N–C bond length changes on the order of 0.01 Å), the GIPAW DFT calculations of the nitrogen magnetic shielding for these systems are consistent with the observed trend: the  $\Delta\delta$  value (i.e., the change in chemical shifts) between **1a-2H<sub>2</sub>O** and **P3** is +2.3 ppm. The computations also indicate that **P5** should possess the most positive chemical shift of the trio, also in accord with experimental findings. As well, the calculated span values for the nitrogen shift tensor are consistent with the experimental limits discussed above (all  $\Omega < 20$  ppm), and change very minimally if we compare **1a-2H<sub>2</sub>O** with either **P3** or **P5**. Overall, the qualitative trends in the nitrogen chemical shift values observed experimentally are reproduced computationally.

In addition to the modest changes in the nitrogen chemical shift values upon complex formation, for the compounds which contain some form of substituted benzene derivative (i.e., **2b**, **3b**, and **4b**), the carbon atom directly attached to the halogen bond donor atom is observed to be dramatically affected upon product formation. For the carbon atom in question, the effect was monitored by comparing the  $^{13}\text{C}$  iso-

tropic chemical shift values for the appropriate starting/product material pairs. The change in the carbon chemical shift is consistently observed to be in the paramagnetic direction (i.e., positive shifts) upon complex formation.<sup>[63b]</sup> For the specific comparison of compound **3b** with complex **P3** (Figure 6), even though the <sup>13</sup>C NMR signal of the carbon

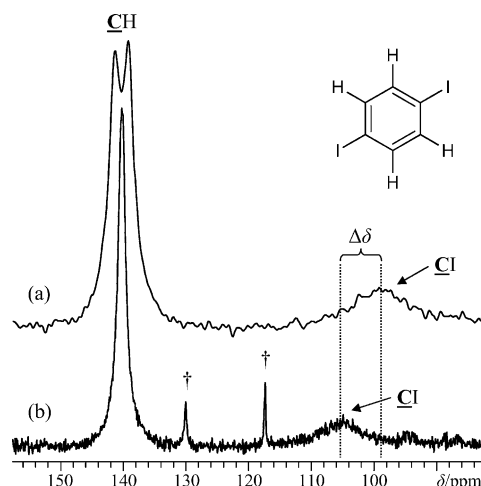


Figure 6. Partial <sup>13</sup>C[<sup>1</sup>H] RAMP-CP/MAS NMR spectra of: a) **3b**, and b) **P3**, which serve to demonstrate the notable change in the carbon chemical shift upon the formation of the supramolecular complex for the carbon atom that is directly attached to the iodine atom. Both systems in this example contain the *p*-diiodobenzene molecule (inset). The iodine atoms in **P3** participate in a halogen bond, whereas there is no such interaction in **3b**. The change in the carbon chemical shift for the iodine-bound carbon (CI) upon complex formation is about +6 ppm, as specified by “ $\Delta\delta$ ”. Daggers indicate MAS spinning sidebands from other carbon sites. For the complete <sup>13</sup>C MAS NMR spectra, see the Supporting Information, Figures S3 to S5.

bound directly to the iodine is rather broad (very likely due to residual dipolar coupling to the quadrupolar <sup>127</sup>I nucleus under MAS), the shift upon product complex formation ( $\Delta\delta_{\text{iso}}$ ) can be estimated as about +6 ppm. A similar observation is made when comparing the appropriate carbon atom chemical shift values between compound **2b** and complex **P2** ( $\Delta\delta_{\text{iso}} = +5.3$  ppm, see the Supporting Information, Figure S3–S5 for all additional <sup>13</sup>C NMR spectra, as well as the tabulated shifts in Table 1). This trend is again opposite to what has been observed using the liquid-state <sup>14</sup>N NMR data mentioned earlier, in which the change in the chemical shift of the nitrogen atom involved in a halogen bond (i.e., the nitrogen atom in quinuclidine with the iodine atom from 1-iodoperfluoropropane) was –7 ppm when compared to the starting material.<sup>[63a]</sup> Halogen bonds involving bromine atoms as the donor are generally considered to be weaker than those involving iodine, and hence it is interesting to note that  $\Delta\delta_{\text{iso}}$  for the **4b/P4** duo is more modest than in both the cases in which iodine is the donor. In the Supporting Information, we also outline how for **4b**, this carbon signal may give detailed information on the <sup>79/81</sup>Br electric field gradient (EFG) tensor, if the peak is broadened by residual dipolar coupling to the <sup>79/81</sup>Br nuclei (see the Support-

ing Information, additional experimental discussion and Figure S5). It is also quite important to note that the chemical shift of the carbon atoms in the ring systems which are not directly attached to the bromine/iodine atom do not appear to change very significantly (on the order of 1 ppm, although this is difficult to quantify) upon formation of the co-crystal product complex.

In order to comment upon the mechanism (i.e., origin) of the significant change in the isotropic carbon shift value of the carbon atom directly bound to a very heavy halogen atom (i.e., Br/I), ZORA DFT quantum chemical calculations were carried out on a model system based upon the *p*-diiodobenzene molecule (as outlined in detail in the Experimental Section), since unambiguous and high-quality X-ray diffraction and SSNMR data are available for both **3b** and **P3**. By analyzing the accepted crystal structure<sup>[65,66]</sup> of the *p*-diiodobenzene molecule in **3b**, it is seen that the carbon–iodine bond length,  $r(\text{C–I})$ , is 2.0911(52) Å. We note here that there appears to be some slight variation in this parameter as a result of the preparation method, as other modern X-ray diffraction studies establish a slightly shorter length of 2.05(1) Å.<sup>[67]</sup> In the product complex **P3**, it is seen that  $r(\text{C–I}) = 2.1093(35)$  Å; hence, this can be reasonably taken as an indication that there is a halogen bond in **P3** involving the iodine atom, which results in lengthening the C–I bond. At the same time, other structural changes in the *p*-diiodobenzene molecule upon the formation of **P3** appear to be very modest (i.e., largely within the measurement errors).

As it appears the change in the C–I bond length is the primary difference between the *p*-diiodobenzene molecule in **3b** and the same molecule in **P3**, ZORA DFT calculations of the magnetic shielding at the carbon and iodine nuclei were performed using a variety of  $r(\text{C–I})$  values near the known structural values; the results for <sup>13</sup>C are displayed in Figure 7. The ZORA DFT computational results are clearly in accord with the experimental observations made using XRD and solid-state <sup>13</sup>C NMR spectroscopy. That is, an increased  $r(\text{C–I})$  bond length will lead to a more positive carbon chemical shift. As well as reproducing the observed trend, the ZORA DFT computations are also in semiquantitative agreement with the experimental observations (i.e., a change in the bond distance of +0.01 Å results in a change of the carbon shift of +0.88 ppm), especially when noting that the  $r(\text{C–I})$  value can vary slightly due to the preparation method of **3b**. In fact, if the  $r(\text{C–I})$  value of 2.05 Å is correct then the results are nearly in quantitative agreement. In addition, the originating mechanism for the changes in the observed <sup>13</sup>C chemical shifts were found using the ZORA DFT method to be due to both increases in paramagnetic shielding (i.e., symmetry-allowed wave function overlap),<sup>[68]</sup> as well as due to relativistic spin-orbit effects.

**Solid-state <sup>14</sup>N NMR spectroscopy:** Unlike the <sup>15</sup>N nuclide, the <sup>14</sup>N nuclide is quadrupolar ( $I = 1$ ), and as such it may be used as a local probe of the EFG in the majority of the systems considered in this study. In contrast with the central-transition solid-state NMR spectra associated with the more



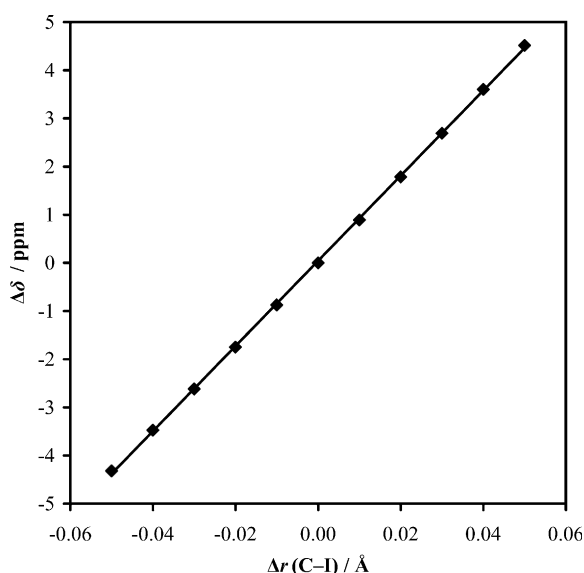


Figure 7. Plot of the ZORA DFT-calculated variation in the  $^{13}\text{C}$  chemical shift value which results from changing the C–I bond distance, where the zero point (i.e.,  $\Delta r = 0.00 \text{ \AA}$ ) has been arbitrarily taken to be the accepted value for pure  $p\text{-C}_6\text{H}_4\text{I}_2$ . For the calculation, an isolated molecule of  $p\text{-C}_6\text{H}_4\text{I}_2$  was used. The data were fit using the linear equation:  $\Delta\delta_{\text{iso}}/\text{ppm} = 88.4(\Delta r/\text{\AA}) + 0.04$ ;  $R^2 = 0.9999$ .

common half-integer quadrupolar nuclei (i.e.,  $I = n/2$ ,  $n = 3, 5, 7, 9$ ), the single-quantum solid-state NMR spectra of integer spin quadrupolar nuclides are broadened by the first-order quadrupolar interaction. As such, even very slight distortions/deviations from tetrahedral symmetry about the central nitrogen atom should be readily observable in the  $^{14}\text{N}$  SSNMR spectra. At the same time, it is fully expected that the symmetry about the nitrogen atoms in the systems considered herein is not distorted to such an extent that more advanced techniques, such as the DEISM approach,<sup>[49]</sup> would be necessary. The spectra displayed in Figure 8 and Figure 9 were acquired in a very straightforward manner with little experimental optimization, although we note here that the direct detection of  $^{14}\text{N}$  NMR in the solid state is far from trivial in general.<sup>[52]</sup> Once again, it is stressed that this can be done as the first-order quadrupolar interaction, while indeed non-zero, does not greatly exceed what can be uniformly excited with a single r.f. transmitter setting.

Even a cursory glance at the  $^{14}\text{N}$  solid-state MAS NMR spectra in Figure 8, Figure 9, and Figure S6 (in the Supporting Information) makes it abundantly clear that there is a significant change in the  $C_Q(^{14}\text{N})$  value upon formation of these supramolecular complexes. Although only five product systems were studied, it was consistently observed that the nitrogen  $C_Q$  value decreased upon formation of the supramolecular framework. For example, the  $^{14}\text{N}$   $C_Q$  of the starting material **2a**·**2H<sub>2</sub>O** was observed to be 72(3) kHz, whereas the product material **P5** has a  $C_Q(^{14}\text{N})$  value of only 39(2) kHz, a reduction of nearly 50 %.

Additional relevant  $^{14}\text{N}$  SSNMR parameters for the materials studied here are in Table 4, and were established using the SIMPSON program.<sup>[69]</sup> It was found that the SIMPSON simulations, which included the effects due to finite radiofrequency pulses, resulted in a slight improvement between the experimental and simulated  $^{14}\text{N}$  SSNMR spectra. Although we were able to reach very satisfactory fits between the experimental data and numerical SIMPSON simulations in nearly all of the nitrogen-containing compounds studied herein, we could not achieve a highly accurate fit for the  $^{14}\text{N}$  data of complex **1a**·**2H<sub>2</sub>O**. At the same time, due to the drastic reduction in the  $C_Q(^{14}\text{N})$  values upon product complex formation, our estimate of  $C_Q(^{14}\text{N})$  for sample **1a**·**2H<sub>2</sub>O** (i.e., ~85 kHz, as further justified in the Supporting Information, Figure S6) is still very distinct from the value obtained upon formation of the product materials **P1** through **P4** (where for all product materials in that series  $C_Q(^{14}\text{N}) \leq 50 \text{ kHz}$ ). Due to the rapid manner in which these particular  $^{14}\text{N}$  MAS experiments may be performed (i.e., minimal experimental set-up and experiment times under 24 h), this

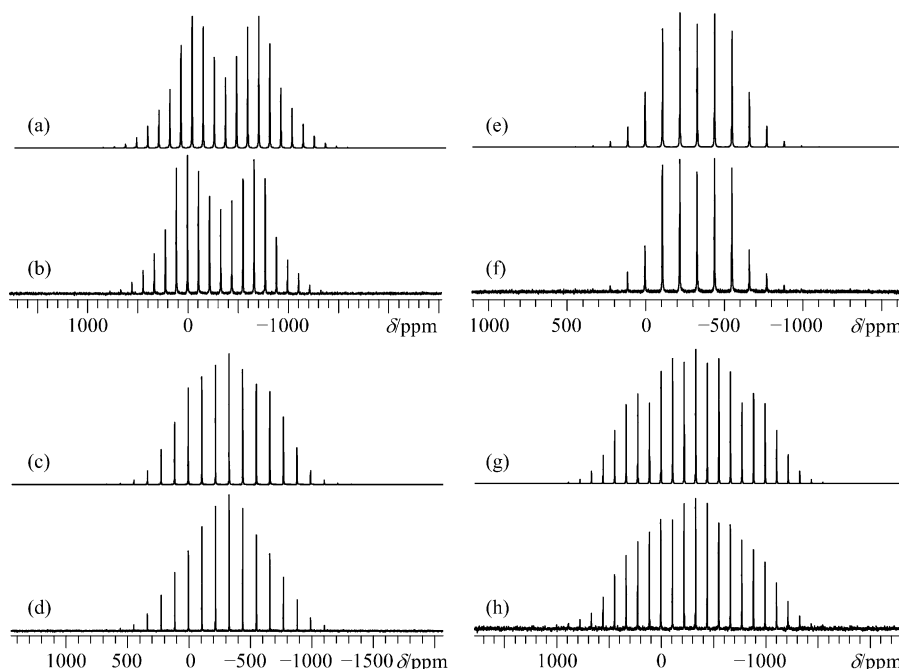


Figure 8. a), c), e), g) Best-fit numerical SIMPSON simulations, and b), d), f), h) experimental  $^{14}\text{N}$  MAS NMR spectra of **P1** (a, b), **P2** (c, d), **P3** (e, f), and **P4** (g, h). For all spectra,  $\nu_{\text{MAS}} = 4 \text{ kHz}$ . Simulation parameters may be found in Table 4.

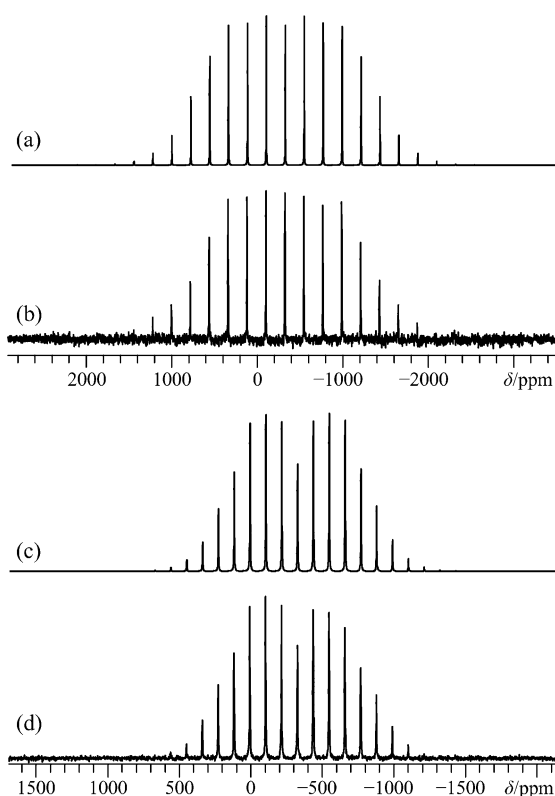


Figure 9. a), c) Best-fit numerical SIMPSON simulations, and b), d) experimental  $^{14}\text{N}$  MAS NMR spectra of **2a·2H<sub>2</sub>O** (a, b) and **P5** (c, d). For the spectra in (a) and (b),  $\nu_{\text{MAS}} = 8$  kHz, whereas for (c) and (d),  $\nu_{\text{MAS}} = 4$  kHz. Simulation parameters may be found in Table 4.

Table 4. Experimental  $^{14}\text{N}$  and  $^{127}\text{I}$  SSNMR data for the systems herein.<sup>[a]</sup>

Compound	$ C_Q(^{14}\text{N}) $ [kHz]	$\eta_Q(^{14}\text{N})$	$ C_Q(^{127}\text{I}) $ [MHz]	$\eta_Q(^{127}\text{I})$	$\delta_{\text{iso}}(^{127}\text{I})$ [ppm]
<b>1a·2H<sub>2</sub>O</b>	ca. 85	ca. 0.5	49.2(0.5)	0.97(0.03)	250(30)
<b>2a·2H<sub>2</sub>O</b>	72(3)	0.51(0.03)	48(2)	0.19(0.05)	250(60)
<b>P1</b>	47(3)	0.25(0.05)	—	—	—
<b>P2</b>	34(3)	0.56(0.04)	—	—	—
<b>P3</b>	24(2)	0.50(0.05)	84.8(0.6)	0.04(0.02)	380(40)
<b>P4</b>	50(3)	0.62(0.05)	—	—	—
<b>P5</b>	39(2)	0.40(0.04)	—	—	—

[a] Measurement errors are within parentheses. Iodine chemical shifts were referenced indirectly to infinitely dilute  $\text{I}^-(\text{aq})$  using solid KI ( $\delta_{\text{iso}} = 192.62$  ppm). Additional information and data acquisition details may be found in the Experimental Section and in the Supporting Information.

suggests that  $^{14}\text{N}$  SSNMR experiments may hold promise in the characterization of these types of systems in the solid state. These changes in the  $C_Q(^{14}\text{N})$  values are very pronounced, especially when compared to the rather modest changes in the nitrogen chemical shift values. By combining the observations from the  $^{14}\text{N}$  and  $^{15}\text{N}$  SSNMR measurements, it is rather clear that the local bonding environments about the nitrogen atoms are not undergoing substantial changes upon complex formation (as quantified by the very modest changes in the nitrogen chemical shift tensor), but that there is a drastic change in the electric field gradient, a

property which possesses a larger degree of nonlocal character. In order to briefly assess if this decrease in the  $C_Q(^{14}\text{N})$  values can be reproduced using quantum chemical computations, we invoked the GIPAW DFT method for the **1a·2H<sub>2</sub>O**, **P3**, and **P5** systems to calculate the nitrogen-14 EFG tensor (Table 2 and the Supporting Information, Table S9). Although the computed values are clearly high relative to the observed values (e.g., the computed  $|C_Q(^{14}\text{N})|$  for **1a·2H<sub>2</sub>O** is 126 kHz, whereas experimentally about 85 kHz is measured), the rather significant reduction in the  $^{14}\text{N}$   $C_Q$  values upon product formation is computationally reproduced, as are the observed trends in the  $C_Q(^{14}\text{N})$  values (i.e.,  $|C_Q(^{14}\text{N}, \mathbf{1a\cdot 2H_2O})| > |C_Q(^{14}\text{N}, \mathbf{P5})| > |C_Q(^{14}\text{N}, \mathbf{P3})|$ ). Based on the crystal structures obtained for **P2**, **P3**, and **P4** as part of this study, it is quite possible that the overestimation in the calculated  $C_Q(^{14}\text{N})$  values relative to the experimental values results from the dynamic motion of the trimethylammonium fragment, as observed previously in *n*-alkyltrimethylammonium bromides by Alonso et al.<sup>[70]</sup> We note that due to the small magnitude of the EFGs at the nitrogen nuclei in all samples, it is likely that the contributions to the EFG are sufficiently nonlocal (scale as  $1/r^3$ ). This is supported by the small changes in the nitrogen chemical shifts across all samples studied, as contributions to chemical shifts are much more local in nature (scale as  $1/r^6$ ) and would, therefore, be a sensitive probe of subtle local changes in electronic structure. To more accurately model the nonlocal EFG contributions, quantum chemical computations which include dispersion effects may very well prove to be fruitful; however, such computations are beyond our present capabilities.

**Solid-state  $^{127}\text{I}$  NMR spectroscopy:** Recently, the SSNMR group at Ottawa has been engaged in the study of the effects that halogen bonding has upon SSNMR parameters using a variety of multinuclear ( $^{35}\text{Cl}$ ,  $^{77}\text{Se}$ ,  $^{81}\text{Br}$ , and  $^{127}\text{I}$ ) magnetic resonance experiments and complementary quantum chemical calculations.<sup>[48,71]</sup> In some cases, it has proven to be rather difficult to isolate the effects of halogen bonding from those of the equally important hydrogen bonding, which tends to also occur in the systems studied to date. As well, it is unfortunate that the direct NMR observation of the halogen atom involved in the halogen bond is expected to be technically challenging, even when employing very high static magnetic fields in combination with advanced pulse sequences. This is because  $C_Q(^{127}\text{I})$  values for covalent iodine atoms are known to range from 1700 to 2000 MHz,<sup>[72]</sup> which is 1–2 orders of magnitude larger than typical  $C_Q$  values measured by solid-state NMR for iodide anions. At the same time, it is noted that  $^{127}\text{I}$  NQR measurements have been used to show that a modest decrease occurs in the  $^{127}\text{I}$  NQR resonance frequencies of the iodine donor atom upon the formation of a halogen bonded complex.<sup>[73]</sup> NQR experiments of this sort occur at rather high resonance frequencies, which are currently beyond our technical capabilities; however, it is clear from the discussion of the  $^{13}\text{C}$  SSNMR results above that the carbon directly bound to



the iodine could very likely serve as an indirect probe of the donor iodine atom. We also note in passing that  $^{129}\text{I}$  Mössbauer measurements can be used to establish the  $C_Q$  values for covalently-bonded iodine atoms.<sup>[74]</sup> Fortunately, directly probing the covalently bound halogen atom is not the only fashion in which one could go about characterizing halogen bonding. Indeed, many examples exist in which the halogen bond acceptor moiety is a halide anion, and in this section we briefly outline the attempts made to characterize these supramolecular materials by  $^{127}\text{I}$  SSNMR experiments which are selective to the iodide anion.

Although a great effort was made to measure the  $^{127}\text{I}$  SSNMR spectra for all of the iodide-containing materials presented as part of this study, only the product complex **P3** yielded  $^{127}\text{I}$  SSNMR spectra which could be meaningfully analyzed and samples **P1**, **P2**, **P4** and **P5** gave no discernible  $^{127}\text{I}$  NMR signal, even after 24 h of data acquisition at  $B_0 = 21.1$  T. Likewise,  $^{127}\text{I}$  NQR experiments were performed on sample **P5**, but also gave no resonance signal over the frequency range from 90 to 130 MHz. Difficulties in obtaining  $^{127}\text{I}$  NMR spectra for many of the product complexes likely stem from a sufficiently distorted electronic environment about the halide anion, which would lead to increased  $C_Q$  values and hence increased line shape broadening. In addition to making intuitive sense (i.e., that a unidirectional halogen bond would lead to a decrease in the spherical symmetry about the halide anion), the possibility is also consistent with the results of GIPAW DFT computations for the  $^{127}\text{I}$  EFG tensors for **1a·2H<sub>2</sub>O**, **P3**, and **P5** (Table 3). To further validate this idea, additional GIPAW DFT computations of the  $^{127}\text{I}$  EFG tensor parameters were performed for the product material **P3**. Keeping everything else within the unit cell constant, the distance between the iodine atom and the iodide anion was varied about the accepted value of 3.522 Å. The results of these calculations are depicted in Figure 10 and clearly show that there is a sensitivity in the  $C_Q(^{127}\text{I})$  parameter as a function of the iodine–iodide distance and is such that a stronger halogen bond (manifested in a shorter iodine–iodide distance) would lead to a larger  $C_Q(^{127}\text{I})$  value at the iodide anion site.

Where high-quality  $^{127}\text{I}$  SSNMR spectra could be acquired, the information obtained using analytical line shape modeling can be found in Table 4, and the spectra are given in Figure 11 and Figure 12. The availability of the high  $B_0$  (i.e., 21.1 T) has greatly facilitated the observation of these  $^{127}\text{I}$  SSNMR spectra, as the broadening associated with the second-order quadrupolar interaction scales inversely with the applied field.<sup>[75]</sup> It is noted that the observed  $C_Q(^{127}\text{I})$  and  $\delta_{\text{iso}}$  values fall within the range previously observed for iodide anions which are participating in a halogen bond.<sup>[48]</sup> It was disappointing that we could only observe the  $^{127}\text{I}$  NMR spectrum of one product material, **P3**. Interestingly, there appears to be a drastic change in the iodine-127  $C_Q$  value between **P3** and all other product materials, which is rather perplexing, especially as the structural changes should be somewhat modest. In all cases there is a bis(trimethylammonium)alkane diiodide and a  $\text{C}_6\text{X}_2\text{Y}_4$  ( $\text{X} = \text{Br}, \text{I}$ ;

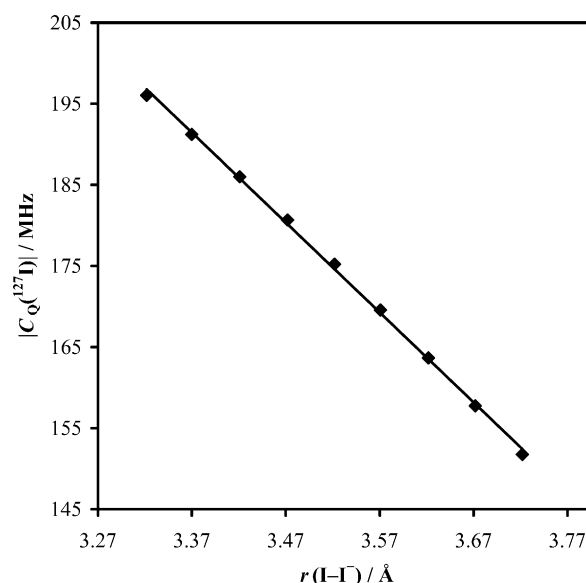


Figure 10. Plot of the GIPAW DFT-calculated variation of the  $|C_Q(^{127}\text{I})|$  value as a function of the iodine–iodide distance for **P3**. The accepted value associated with the crystal structure is  $r(\text{I}-\text{I}^-) = 3.522$  Å. Prior to the NMR parameter calculation, the hydrogen atoms were geometry-optimized starting from the accepted crystal structure. The data were fit using the linear equation:  $|C_Q(^{127}\text{I})|/\text{MHz} = -110.87(r/\text{\AA}) + 565.08$ ;  $R^2 = 0.9989$ .

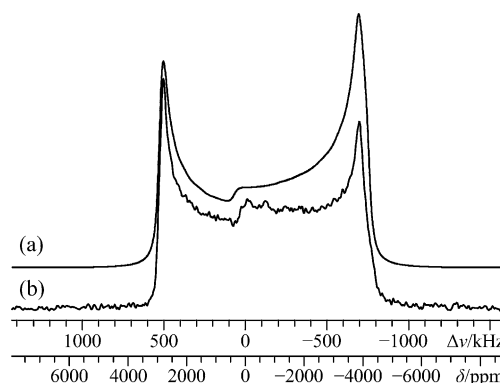


Figure 11. a) Best-fit analytical WSolid simulation, and b) experimental VOS Solomon echo  $^{127}\text{I}\{^1\text{H}\}$  NMR spectrum of **P3**, acquired at  $B_0 = 21.1$  T. Simulation parameters may be found in Table 4.

$\text{Y} = \text{H}, \text{F}$ ) unit assembled in a 1:1 stoichiometry. However, studies on molecules which participate in halogen bonding show that the local environment about the donor halogen atom can be significantly modified by simply changing the identity of the substituents on a substituted benzene ring.<sup>[76]</sup> Upon performing  $^{127}\text{I}$  SSNMR experiments on the starting materials **1a·2H<sub>2</sub>O** and **2a·2H<sub>2</sub>O**, it became clear to us that the iodine environments in **1a·2H<sub>2</sub>O** and **P3** were entirely different, which lends even further support (in addition to  $^{13}\text{C}$ ,  $^{14}\text{N}$ , and  $^{15}\text{N}$  NMR) that the local electronic environment about the iodide anion had drastically changed upon formation of the co-crystal product materials.

It is noted in passing that we did not attempt to include iodine chemical shift anisotropy in any of our line shape fit-

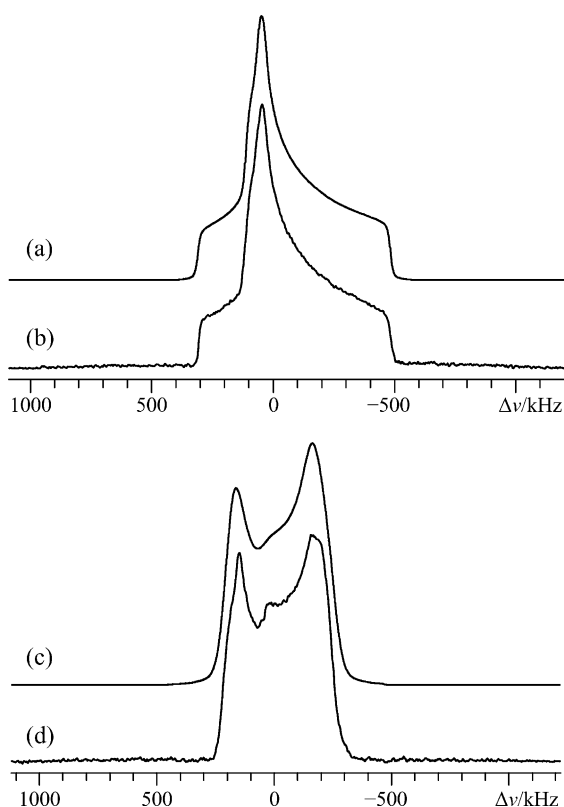


Figure 12. a), c) Best-fit analytical WSolids simulations, and b), d) experimental VOCS Solomon echo  $^{127}\text{I}\{^1\text{H}\}$  NMR spectra of **1a**·**2H<sub>2</sub>O** (a, b) and **2a**·**2H<sub>2</sub>O** (c, d), acquired at  $B_0=21.1$  T. Simulation parameters may be found in Table 4.

ting models, due to: 1) the difficulty in obtaining high-quality  $^{127}\text{I}$  SSNMR data at two applied fields, and 2) the rather small effect that the shift anisotropy would have on the total iodine NMR line width. Preliminary data were acquired for **1a**·**2H<sub>2</sub>O** and **P3** at a lower field as part of an effort to substantiate the iodine shift anisotropy, and although the observed  $^{127}\text{I}$  NMR line shapes were consistent with the EFG tensor parameters measured at 21.1 T, the data quality was not high enough at the lower  $B_0$  to accomplish this objective (Supporting Information, Figure S7). On the basis of the results presented here, it appears that the halogen bond creates such a large distortion in the electronic symmetry about the halide so as to render  $^{127}\text{I}$  SSNMR experiments infeasible, even at very high applied magnetic field strengths. Disorder in some of the compounds, as shown crystallographically (vide supra), also likely plays a role. Potential remedies to this could appear in the future due to the development of even higher  $B_0$  strengths, advances in NMR pulse sequence design, or potentially by performing the measurements at very low temperatures, which is known to increase the nuclear spin polarization (and hence experimental sensitivity). As noted earlier in a study on haloanilinium halides,<sup>[48]</sup> it is believed that chemical shift anisotropy information might prove useful in determining the complex interplay between the halogen and hydrogen bonding observed in many of

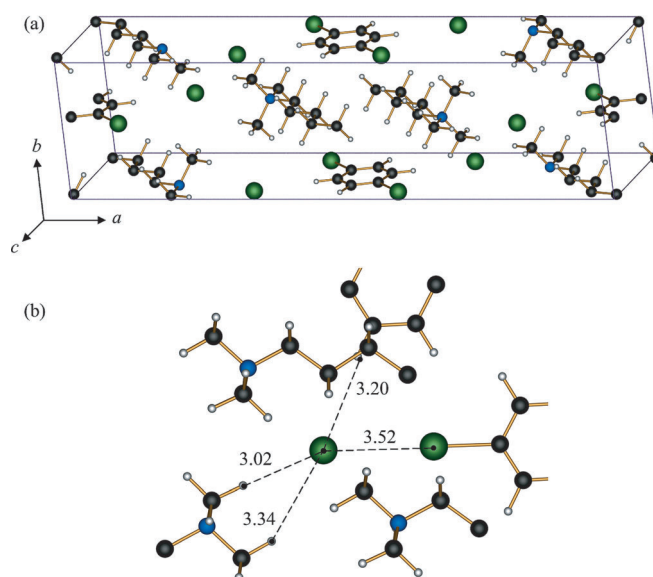


Figure 13. POV-ray renderings of: a) the unit cell, and b) the local structure about the iodide anions for the product material **P3**. The following color and labeling scheme is used: I=green; N=blue; C=black; H=white. b) The black dashed lines highlight some of the important interactions within 3.52 Å of the iodide anion (the internuclear distances [Å] are specified near the dashed lines). Within this distance, there are ten H contacts (three highlighted), and one halogen bond with the iodine atom from an adjacent *p*-diiodobenzene molecule.

these materials (Figure 13), although the practical measurement of this is very difficult, as noted above.

**Solid-state  $^{19}\text{F}$  NMR spectroscopy:** Based on the structures proposed from refined X-ray diffraction data of **P2** and **P4**, there was reason to suspect dynamic structural disorder of the *p*-C<sub>6</sub>F<sub>4</sub>I<sub>2</sub> ring moiety. The physical rationale is rather simple: as the C<sub>6</sub>F<sub>4</sub>I<sub>2</sub> molecule cannot participate in strong hydrogen bonding (compare with, for example, **P3**), and as it is thought to be experiencing a halogen bond via the iodine atom, it should be free to rotate about the C<sub>2</sub> molecular axis, which is parallel to the C–I bond vector. As the environments experienced by the  $^{19}\text{F}$  nuclei would be rather sensitive to this motion,  $^{19}\text{F}$  NMR experiments were carried out under (primarily) MAS conditions for samples **P2** and **P4**, as well as the starting materials **2b** and **4b**.

The observed  $^{19}\text{F}$  MAS NMR spectra for **P2** and **P4** are rather similar to one another (Figure 14); however, it was interesting to note that two isotropic peaks could be observed. It is noted here that due to technical limitations, we could not attempt any homonuclear decoupling experiments<sup>[77]</sup> and hence the resolution afforded in the presented  $^{19}\text{F}$  NMR spectra is due to MAS averaging effects only. Additional  $^{19}\text{F}$  MAS NMR experiments were performed on **2b** and **4b**, in which halogen bonding should be absent. It is seen that the resonances in the  $^{19}\text{F}$  NMR spectra of the product materials are shifted in the diamagnetic direction relative to the starting materials, although we cannot quantify the effect as we cannot unambiguously assign the observed peaks to sites in the chemical structure. The observed

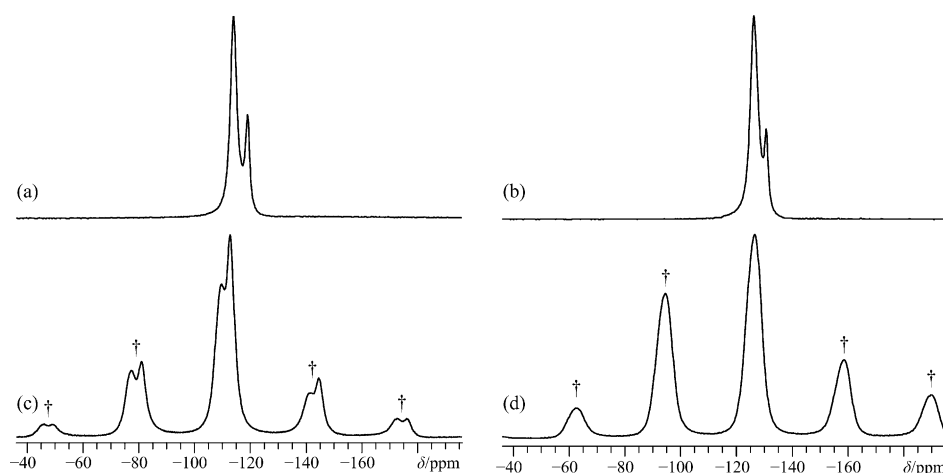


Figure 14. Experimental  $^{19}\text{F}$  MAS NMR spectra of: a) **P2**, b) **P4**, c) **2b**, and d) **4b**. All experimental data were acquired at ambient temperature. The spectra in (a, b) used  $\nu_{\text{MAS}} = 25.0$  kHz, whereas the spectra in (c, d) used  $\nu_{\text{MAS}} = 12.0$  kHz. Spinning sidebands are labeled with daggers.

shifts are rather interesting considering that very minimal structural changes should be occurring proximate to the  $^{19}\text{F}$  nuclei; however, we note that diamagnetic shifts upon the formation of a halogen bond are consistent with the  $^{19}\text{F}$  NMR data for *p*-diiodotetrafluorobenzene in a variety of coordinating solvents.<sup>[78]</sup> The variable-temperature  $^{19}\text{F}$  NMR spectra of **P2** and **P4** (see the Supporting Information, Figures S8 and S9) are insensitive to temperature, other than some very small shift changes ( $< 2$  ppm over the full range of temperature). There are no discernible line width changes in this temperature range, which suggests that dynamic disorder of the rings is unlikely. The  $^{19}\text{F}$  SSNMR data appear to be consistent with the XRD results: the substituted rings in **P2** and **P4** can be represented by two structures: one where the fluorine atoms of the ring interact weakly with the hydrogen atoms near the middle of the long alkyl chains (i.e., the  $\delta$  and  $\epsilon$  positions, as specified in Scheme 2), and one where such an interaction is not present. Although not a commonly exploited motif in crystal engineering, the existence of  $\text{C-H}\cdots\text{F}$  interactions is not novel.<sup>[79]</sup> We note further that in only the  $^{13}\text{C}$  NMR spectra for **P2** and **P4** do we observe carbon chemical shifts at about 30 ppm, in addition to the expected signal for these carbon environments at ca. 32 ppm, which provides further evidence for a type of  $\text{C-H}\cdots\text{F}$  interaction.

## Conclusion

By combining high-quality multinuclear ( $^{13}\text{C}$ ,  $^{14/15}\text{N}$ ,  $^{19}\text{F}$ ,  $^{127}\text{I}$ ) solid-state magnetic resonance data with computational modeling and X-ray diffraction measurements, we demonstrated that halogen bonding, as well as supramolecular structure formation itself, can significantly affect several different NMR observables in the solid state. Carbon-13 solid-state NMR experiments can be used to rapidly determine sample purity; however, by carefully considering the chemi-

cal shift values of the carbon atom directly adjacent to the halogen bond donor (i.e., the bromine or iodine) it is clear that the halogen bond results in increasing the  $^{13}\text{C}$  chemical shift at this carbon. For the systems studied herein, this augmentation in the carbon shift appears to be on the order of +5 to +6 ppm for systems in which the iodine atom acts as the donor, whereas the change is more modest in the case in which a bromine atom is the donor (ca. +2.5 ppm). This change is readily modeled and supported by quantum chemical computations that include relativistic effects. As observed

by X-ray diffraction, the primary structural change associated with the changing carbon chemical shift is an increase in the C–X bond distance upon the establishment of a halogen bond.

Nitrogen-14/15 solid-state NMR experiments upon these materials were used to assess the impact of structural changes upon the NMR probe nuclei for sites which are not directly involved in the halogen bond. We observed a small systematic paramagnetic shift (i.e., deshielding) in the  $\delta_{\text{iso}}$  ( $^{15}\text{N}$ ) value upon complex formation (on the order of 1 to 2 ppm), which was supported by GIPAW DFT calculations. This subtle change in the nitrogen chemical shifts is consistent with the small local structural perturbations which are occurring upon product formation, as supported by X-ray diffraction measurements. Intriguingly, although the  $^{15}\text{N}$  chemical shift perturbations were modest, changes in the  $C_Q(^{14}\text{N})$  values upon product formation were significant and such that the product materials exhibited a reduced  $C_Q$  value. Relative to chemical shifts, which (through magnetic shielding) are local probes of electronic structure, changes in the  $^{14}\text{N}$   $C_Q$  values should be more sensitive to structural changes which are occurring further away from the probe nucleus. Once again, the reduction in  $C_Q(^{14}\text{N})$  values upon product formation is consistent with the trends observed from GIPAW DFT calculations.

Although both  $^{35/37}\text{Cl}$  and  $^{79/81}\text{Br}$  SSNMR measurements have been used in the past to comment upon halogen bond formation,<sup>[48]</sup> observing the same interactions by  $^{127}\text{I}$  SSNMR is a more significant challenge. Use of a very high magnetic field (i.e., 21.1 T) has allowed for some systems to be characterized using  $^{127}\text{I}$  SSNMR, although this could not be done for all samples. Experimental  $^{127}\text{I}$  SSNMR measurements indicate an increase in the  $C_Q(^{127}\text{I})$  value of the iodide anion upon formation of a halogen bond, which makes intuitive sense as the halogen bond should perturb the high electronic symmetry of this anion. Quantum chemical calculations again support this trend, and calculations highlight the

sensitivity of the iodide  $C_0(^{127}\text{I})$  value to the iodine–iodide distance. Lastly, variable-temperature  $^{19}\text{F}$  SSNMR experiments upon several of the systems appear to indicate static, rather than dynamic, disorder in the product materials **P2** and **P4**. A weak intermolecular C–H...F interaction is thought to be partly responsible for this effect, as supported by X-ray diffraction experiments and  $^{13}\text{C}$  chemical shift perturbations of the relevant  $\delta/\epsilon$  carbon atoms.

## Experimental Section

**Co-crystallization procedure and X-ray diffraction experiments:** The halogen-bonded complexes **P1** and **P5** were prepared following previously reported procedures.<sup>[41,62]</sup> Single crystals of **P2**, **P3**, and **P4** were grown by a slow solvent evaporation technique under isothermal conditions at 298 K. In a typical co-crystallization procedure, equimolar amounts of the halogen bond donor and acceptor were separately dissolved at room temperature in a 1:1 chloroform/acetonitrile mixture. The saturated solutions containing the halogen bond donor and acceptor were mixed in a clear borosilicate glass vial, which was left open in a closed cylindrical wide-mouth bottle containing paraffin oil. Solvents were allowed to slowly evaporate at room temperature and to be absorbed by the paraffin oil until crystals were formed in a period ranging from 3 to 5 days. Powdered samples were easily prepared on the scale of hundreds of milligrams.

X-ray diffraction data for **P2**, **P3**, and **P4** were collected on a Bruker-AXS KAPPA-APEX II CCD diffractometer using  $\text{MoK}_\alpha$  radiation,  $\lambda = 0.71073 \text{ \AA}$ , as selected by a graphite monochromator. Room temperature **P2** and **P4** diffraction patterns were characterized by large spot anisotropy and diffuse strikes, indicating extended disorder. Attempts to collect data at a lower temperature failed due to crystal cracking or a phase transition. For **P3** it was possible to collect data at 223 K. Please note that the crystal structures of **P1** and **P5** were previously reported.<sup>[41,62]</sup> Details of the crystallographic data collection, structure solution, and refinement are reported in the Supporting Information.

### Solid-state nuclear magnetic resonance experiments

**General:** Prior to SSNMR experiments, the solid samples were gently powdered and tightly packed into Bruker 4.0 mm outer diameter (o.d.)  $\text{ZrO}_2$  rotors (experiments at  $B_0 = 9.4$  and 11.75 T), 2.5 mm o.d.  $\text{ZrO}_2$  rotors (experiments at  $B_0 = 4.7 \text{ T}$ ), or 4.0/5.0 mm o.d. glass tubes (experiments at  $B_0 = 21.1 \text{ T}$ ). A variety of MAS and static NMR probes were used; specific probe details are outlined in the Supporting Information, Tables S2–S6.

The  $^{13}\text{C}$ ,  $^{14}\text{N}$ ,  $^{15}\text{N}$ , and  $^{19}\text{F}$  SSNMR data were acquired at the University of Ottawa using either a wide bore Bruker AVANCE spectrometer, which operates at  $B_0 = 11.75 \text{ T}$  ( $\nu_0(^1\text{H}) = 500.13 \text{ MHz}$ ;  $\nu_0(^{13}\text{C}) = 125.76 \text{ MHz}$ ;  $\nu_0(^{14}\text{N}) = 36.14 \text{ MHz}$ ;  $\nu_0(^{15}\text{N}) = 50.70 \text{ MHz}$ ) or a wide bore Bruker AVANCE III spectrometer, which operates at  $B_0 = 9.4 \text{ T}$  ( $\nu_0(^1\text{H}) = 400.17 \text{ MHz}$ ;  $\nu_0(^{13}\text{C}) = 100.62 \text{ MHz}$ ;  $\nu_0(^{15}\text{N}) = 40.56 \text{ MHz}$ ;  $\nu_0(^{19}\text{F}) = 376.53 \text{ MHz}$ ). Fluorine-19 SSNMR data were also acquired at the University of Ottawa, but used a wide bore Bruker AVANCE III spectrometer, which operates at  $B_0 = 4.7 \text{ T}$  ( $\nu_0(^{19}\text{F}) = 188.24 \text{ MHz}$ ), in addition to the  $B_0 = 9.4 \text{ T}$  system. For selected systems,  $^{127}\text{I}$  SSNMR data were acquired using a standard bore Bruker AVANCE II spectrometer at the National Ultrahigh-Field NMR Facility for Solids in Ottawa, which operates at  $B_0 = 21.1 \text{ T}$  ( $\nu_0(^1\text{H}) = 899.95 \text{ MHz}$ ;  $\nu_0(^{127}\text{I}) = 180.06 \text{ MHz}$ ).

**$^{13}\text{C}$  NMR experiments:** All  $^{13}\text{C}$  SSNMR spectra were acquired under MAS conditions ( $\nu_{\text{MAS}} = 5.0$  to 12.0 kHz). For samples which contained  $^1\text{H}$  nuclei, the  $^{13}\text{C}$  NMR signal was obtained using the RAMP-CP pulse sequence,<sup>[80]</sup> with  $^1\text{H}$  decoupling during the acquisition period enabled by using either the two pulse phase modulated (TPPM)<sup>[81]</sup> or the 64-step small phase incremental alternation (SPINAL-64)<sup>[82]</sup> method. For selected  $^1\text{H}$ -containing systems direct detection (i.e., no CP) of the  $^{13}\text{C}$  signal was also performed, but did not produce a substantially different final

spectrum (data not shown). Direct detection of the  $^{13}\text{C}$  NMR signal (using either a simple Bloch decay or the Hahn echo experiment)<sup>[83]</sup> was also used for samples which did not contain any  $^1\text{H}$  nuclei. Chemical shift referencing and radiofrequency field strength calibration were established using a powdered sample of glycine under 5 kHz MAS conditions, and is such that the chemical shift of carboxyl group carbon is 176.46 ppm.<sup>[84]</sup> Detailed  $^{13}\text{C}$  SSNMR experimental acquisition parameters may be found in the Supporting Information, Table S2.

**$^{15}\text{N}$  NMR experiments:** Nitrogen-15 SSNMR experiments were carried out under static and MAS conditions ( $\nu_{\text{MAS}} = 4.0$  or 5.0 kHz). All  $^{15}\text{N}$  experiments employed the RAMP-CP pulse sequence, with TPPM  $^1\text{H}$  decoupling during the acquisition period.  $^{15}\text{N}$  chemical shifts were referenced and radiofrequency field strengths were calibrated using the ammonium nitrogen signal from a powdered sample of non-uniformly  $^{15}\text{N}$ -enriched  $^{15}\text{NH}_4\text{NO}_3$  ( $\nu_{\text{MAS}} = 5 \text{ kHz}$ ), and is such that the chemical shift of the ammonium nitrogen is  $-358.45 \text{ ppm}$ <sup>[85]</sup> relative to the  $\text{CH}_3\text{NO}_2$  primary standard (i.e.,  $\delta(^{15}\text{N}, \text{CH}_3\text{NO}_2) \equiv 0 \text{ ppm}$ ). Detailed  $^{15}\text{N}$  SSNMR acquisition parameters may be found in the Supporting Information, Table S3.

**$^{14}\text{N}$  NMR experiments:** All  $^{14}\text{N}$  SSNMR experiments were performed under MAS conditions ( $\nu_{\text{MAS}} = 4.0$  to 8.0 kHz) using an echo pulse sequence<sup>[86]</sup> the timing of which was synchronized with the rotor period. For selected samples, continuous wave (CW)  $^1\text{H}$  decoupling was tested under the conditions outlined above, but was found to produce  $^{14}\text{N}$  NMR spectra which were very similar to those which did not employ decoupling; hence,  $^1\text{H}$  decoupling was not generally employed. In order to acquire the broad  $^{14}\text{N}$  NMR signals of samples **1a-2H<sub>2</sub>O** and **2a-2H<sub>2</sub>O**, the variable offset cumulative spectrum (VOCS)<sup>[87–89]</sup> method was used, and the subspectra obtained were processed as demonstrated in prior accounts.<sup>[48,64,90,91]</sup> To a very good approximation, the  $^{14}\text{N}$  chemical shift values are equivalent to those measured by  $^{15}\text{N}$  MAS NMR experiments, as established previously.<sup>[92]</sup> This is reasonable as nitrogen-14/15 isotope effects on the chemical shift are typically  $\pm 0.3 \text{ ppm}$ ,<sup>[93]</sup> which is well within the chemical shift measurement errors for the  $^{14}\text{N}$  NMR experiments. The radiofrequency field strengths were calibrated using a powdered sample of  $\text{NH}_4\text{Cl}$  under MAS ( $\nu_{\text{MAS}} = 5.0 \text{ kHz}$ ). Advanced methods aimed at calibration of the magic angle setting were not attempted; rather, the common method which uses the  $^{81}\text{Br}$  NMR signal of KBr under MAS was employed.<sup>[94]</sup> Detailed  $^{14}\text{N}$  SSNMR acquisition parameters may be found in the Supporting Information, Table S4.

**$^{127}\text{I}$  NMR experiments:** Iodine-127 SSNMR experiments were performed under static conditions, using the solid (Solomon) echo pulse sequence<sup>[86]</sup> and the VOCS method.<sup>[87–89]</sup> CW  $^1\text{H}$  decoupling was found to not substantially alter the observed  $^{127}\text{I}$  NMR spectra. The iodine radiofrequency field strengths and chemical shift referencing were established using a powdered sample of KI under static conditions ( $\delta_{\text{iso}}(^{127}\text{I}, \text{KI}) = 192.62 \text{ ppm}$ <sup>[44]</sup>). Preliminary  $^{127}\text{I}$  SSNMR spectra were also acquired for samples **P3** and **1a-2H<sub>2</sub>O** at  $B_0 = 11.75$  and 9.4 T, respectively, and are consistent with the data acquired at 21.1 T; however, these spectra were not of high quality, and hence were not used to extract the relevant NMR parameters. Detailed  $^{127}\text{I}$  SSNMR acquisition parameters may be found in the Supporting Information, Table S5.

**$^{19}\text{F}$  NMR experiments:** Spectra were typically acquired under MAS conditions ( $\nu_{\text{MAS}} = 12.0$  to 25.0 kHz), although rather featureless static  $^{19}\text{F}$  NMR spectra were also obtained (data not shown). Variable-temperature  $^{19}\text{F}$  NMR experiments were also attempted at temperatures ranging from 255 to 333 K. All spectra were acquired using the Hahn echo pulse sequence.<sup>[83]</sup> Referencing and radiofrequency field strength calibration were established using liquid  $\text{C}_6\text{F}_6$  at room temperature, and is such that its chemical shift is  $-163.0 \text{ ppm}$  with respect to the accepted primary standard  $\text{CFCl}_3$  (i.e.,  $\delta_{\text{iso}}(\text{CFCl}_3) \equiv 0 \text{ ppm}$ ).<sup>[75]</sup> Detailed  $^{19}\text{F}$  SSNMR experimental acquisition parameters may be found in the Supporting Information, Table S6.

**NMR data analysis:** Isotropic peak positions for the  $^{13}\text{C}$  and  $^{15}\text{N}$  NMR spectra were determined using TOPSPIN 1.3 (Bruker BioSpin), with the reported error bounds established as the breadth of the line shape at 90% of the maximum peak height. Analytical line shape models of the VOCS  $^{127}\text{I}$  SSNMR spectra were achieved using the program WSolids (v.

1.19.11),<sup>[95]</sup> whereas numerical simulations of the  $^{14}\text{N}$  MAS NMR spectra were generated using the SIMPSON<sup>[69]</sup> software package. Additional SIMPSON programming details can be found in the Supporting Information (Additional Experimental and Discussion).

**Quantum chemical calculations:** For selected systems, quantum chemical computations were performed using the GIPAW DFT method, as specified in the CASTEP NMR (v. 4.1) software package.<sup>[53,56,96,97]</sup> Input files were generated with Materials Studio (v. 3.2.0.0), and used either “ultra-soft” or “on-the-fly” generation (otfg) pseudopotentials.<sup>[96,98]</sup> The iodine otfg pseudopotential was obtained from Accelrys Inc. (San Diego, CA), and takes the form reported previously.<sup>[64]</sup> All CASTEP calculations used the generalized gradient approximation (GGA), with the exchange-correlation (XC) functional developed by Perdew, Burke, and Ernzerhof (i.e., PBE).<sup>[99,100]</sup> Prior to all GIPAW DFT calculations of NMR observables, the accepted solid-state crystal structures from either the literature (i.e., **1a**·2H<sub>2</sub>O and **P5**)<sup>[41,62]</sup> or the present study (i.e., **P3**) were subjected to a geometry optimization of the hydrogen positions, as suggested and documented previously.<sup>[101]</sup> Additional GIPAW DFT details can be found in the Supporting Information, Tables S7–S10.

In order to include relativistic effects, the molecular unit of **3b** was selected and subjected to calculations using the ZORA DFT method, as implemented in version 2012.01 of the Amsterdam Density Functional (ADF) software<sup>[102–104]</sup> produced by Scientific Computing and Modelling (SCM). All magnetic shielding computations using the ZORA DFT approach employed the NMR module and included spin-orbit effects<sup>[105]</sup> with all-electron quadruple- $\zeta$  basis sets, which included polarization functions (i.e., QZ4P). The XC functional used in the ZORA DFT computations was as follows: local density approximation (LDA) of Vosko, Wilk, and Nusair (VWN),<sup>[106]</sup> GGA exchange according to the revised correction of Zhang and Yang (revPBE),<sup>[107]</sup> and PBE correlation (PBEc).<sup>[99,100]</sup> The actual  $p\text{-C}_6\text{H}_4\text{I}_2$  molecule used for the ZORA DFT computations was based upon the structure provided by Boese and Miebach,<sup>[66]</sup> but the hydrogen positions were computationally optimized using the CASTEP software as described above.  $D_{2h}$  molecular point symmetry was enforced; this resulted in changing C–C bond lengths maximally by 0.008 Å, but all changes are within the reported measurement errors associated with the X-ray structure. Subsequently, keeping all atoms other than the iodine fixed in space, the C–I bond distance was varied in steps of 0.01 Å to generate Figure 7.

CCDC-926827 (**P2**), -926828 (**P3**) and -926829 (**P4**) contain the supplementary crystallographic data for this paper. These data can be obtained free of charge from The Cambridge Crystallographic Data Centre via [www.ccdc.cam.ac.uk/data\\_request/cif](http://www.ccdc.cam.ac.uk/data_request/cif).

## Acknowledgements

C.M.W. and D.L.B. are grateful to the Natural Sciences and Engineering Research Council (NSERC) for funding and the High-Performance Computing Virtual Laboratory (HPCVL) for computational resources. Access to the 900 MHz NMR spectrometer was provided by the National Ultra-high-Field NMR Facility for Solids (Ottawa, Canada), a national research facility funded by the Canada Foundation for Innovation, the Ontario Innovation Trust, Recherche Québec, the National Research Council Canada, and Bruker BioSpin and managed by the University of Ottawa ([www.nmr900.ca](http://www.nmr900.ca)). NSERC is acknowledged for a Major Resources Support grant. G.C., P.M., and G.R. acknowledge Fondazione Cariplo (projects 2009-2550 and 2010-1351) for financial support.

[1] H. A. Bent, *Chem. Rev.* **1968**, 68, 587–648.

[2] D. Hadži, H. W. Thompson, *Hydrogen Bonding: Papers Presented at the Symposium on Hydrogen Bonding Held at Ljubljana*, July 29–August 3, 1957, Pergamon, London, **1959**.

[3] G. C. Pimentel, A. L. McClellan, *The Hydrogen Bond*, W. H. Freeman and Company, San Francisco, **1960**.

- [4] T. Steiner, *Angew. Chem.* **2002**, 114, 50–80; *Angew. Chem. Int. Ed.* **2002**, 41, 48–76.
- [5] W. C. Hamilton, J. A. Ibers, *Hydrogen Bonding in Solids*, W. A. Benjamin, New York, **1968**.
- [6] F. Cangelosi, M. T. Shaw, *Polym. Plast. Technol. Eng.* **1983**, 21, 13–98.
- [7] G. R. Desiraju, T. Steiner, *The Weak Hydrogen Bond: In Structural Chemistry and Biology*, Oxford University Press, New York, **1999**.
- [8] P. Gamez, T. J. Mooibroek, S. J. Teat, J. Reedijk, *Acc. Chem. Res.* **2007**, 40, 435–444.
- [9] B. L. Schottel, H. T. Chifotides, K. R. Dunbar, *Chem. Soc. Rev.* **2008**, 37, 68–83.
- [10] I. D. Giles, H. T. Chifotides, M. Shatruk, K. R. Dunbar, *Chem. Commun.* **2011**, 47, 12604–12606.
- [11] J. C. Ma, D. A. Dougherty, *Chem. Rev.* **1997**, 97, 1303–1324.
- [12] M. Cametti, A. D. Cort, L. Mandolini, *Chem. Sci.* **2012**, 3, 2119–2122.
- [13] M. Taddei, F. Costantino, R. Vivani, C. Sangregorio, L. Sorace, L. Castelli, *Cryst. Growth Des.* **2012**, 12, 2327–2335.
- [14] M. Egli, S. Sarkhel, *Acc. Chem. Res.* **2007**, 40, 197–205.
- [15] Y. V. Nelyubina, P. Y. Barzilovich, M. Y. Antipin, S. M. Aldoshin, K. A. Lyssenko, *ChemPhysChem* **2011**, 12, 2895–2898.
- [16] M. Nishio, M. Hirota, Y. Umezawa, *The CH– $\pi$  Interaction: Evidence, Nature and Consequences*, Wiley, Weinheim, **1998**.
- [17] C. J. Pace, D. Kim, J. Gao, *Chem. Eur. J.* **2012**, 18, 5832–5836.
- [18] M. J. Plevin, D. L. Bryce, J. Boissbouvier, *Nat. Chem.* **2010**, 2, 466–471.
- [19] M. Bardajia, A. Laguna, *Eur. J. Inorg. Chem.* **2003**, 3069–3079.
- [20] P. Pyykkö, *Angew. Chem.* **2004**, 116, 4512–4557; *Angew. Chem. Int. Ed.* **2004**, 43, 4412–4456.
- [21] I. O. Koshevoy, L. Koskinen, E. S. Smirnova, M. Haukka, T. A. Pakkanen, A. S. Melnikov, S. P. Tunik, *Z. Anorg. Allg. Chem.* **2010**, 636, 795–802.
- [22] C. Estarellas, A. Frontera, D. Quiñero, P. M. Deyà, *ChemPhysChem* **2011**, 12, 2742–2750.
- [23] A. Ebrahimi, M. Habibi, R. S. Neyband, A. R. Gholipour, *Phys. Chem. Chem. Phys.* **2009**, 11, 11424–11431.
- [24] Y. Guo, Y. Ma, N. Zhou, Z.-Q. Liu, Q.-L. Wang, S.-P. Yan, D.-Z. Liao, *Z. Anorg. Allg. Chem.* **2010**, 636, 865–871.
- [25] N. Ma, Y. Zhang, B. Ji, A. Tian, W. Wang, *ChemPhysChem* **2012**, 13, 1411–1414.
- [26] Q. Li, X. Xu, T. Liu, B. Jing, W. Li, J. Cheng, B. Gong, J. Sun, *Phys. Chem. Chem. Phys.* **2010**, 12, 6837–6843.
- [27] A. R. Voth, P. Khuu, K. Oishi, P. S. Ho, *Nat. Chem.* **2009**, 1, 74–79.
- [28] P. Metrangolo, G. Resnati, *Chem. Eur. J.* **2001**, 7, 2511–2519.
- [29] P. Metrangolo, F. Meyer, T. Pilati, G. Resnati, G. Terraneo, *Angew. Chem.* **2008**, 120, 6206–6220; *Angew. Chem. Int. Ed.* **2008**, 47, 6114–6127.
- [30] G. Cavallo, P. Metrangolo, T. Pilati, G. Resnati, M. Sansotera, G. Terraneo, *Chem. Soc. Rev.* **2010**, 39, 3772–3783.
- [31] G. Cavallo, S. Biella, J. Lü, P. Metrangolo, T. Pilati, G. Resnati, G. Terraneo, *J. Fluorine Chem.* **2010**, 131, 1165–1172.
- [32] F. Guthrie, *J. Chem. Soc.* **1863**, 16, 239–244.
- [33] I. Remsen, J. F. Norris, *Am. Chem. J.* **1896**, 18, 90–96.
- [34] P. Politzer, P. Lane, M. C. Concha, Y. Ma, J. S. Murray, *J. Mol. Model.* **2007**, 13, 305–311.
- [35] A. Priimagi, M. Saccone, G. Cavallo, A. Shishido, T. Pilati, P. Metrangolo, G. Resnati, *Adv. Mater.* **2012**, 24, OP345–OP352.
- [36] E. Cariati, G. Cavallo, A. Forni, G. Leem, P. Metrangolo, F. Meyer, T. Pilati, G. Resnati, S. Righetto, G. Terraneo, E. Tordin, *Cryst. Growth Des.* **2011**, 11, 5642–5648.
- [37] E. Parisini, P. Metrangolo, T. Pilati, G. Resnati, G. Terraneo, *Chem. Soc. Rev.* **2011**, 40, 2267–2278.
- [38] R. Berger, G. Resnati, P. Metrangolo, E. Weber, J. Hulliger, *Chem. Soc. Rev.* **2011**, 40, 3496–3508.
- [39] M. Erdélyi, *Chem. Soc. Rev.* **2012**, 41, 3547–3557.
- [40] P. Politzer, J. S. Murray, T. Clark, *Phys. Chem. Chem. Phys.* **2010**, 12, 7748–7757.

- [41] P. Metrangolo, Y. Carcenac, M. Lahtinen, T. Pilati, K. Rissanen, A. Vij, G. Resnati, *Science* **2009**, 323, 1461–1464.
- [42] D. L. Bryce, G. D. Sward, *Magn. Reson. Chem.* **2006**, 44, 409–450.
- [43] C. M. Widdifield, R. P. Chapman, D. L. Bryce, *Annu. Rep. Nucl. Magn. Reson. Spectrosc.* **2009**, 66, 195–326.
- [44] R. P. Chapman, C. M. Widdifield, D. L. Bryce, *Prog. Nucl. Magn. Reson. Spectrosc.* **2009**, 55, 215–237.
- [45] B. J. Butler, J. M. Hook, J. B. Harper, *Annu. Rep. Nucl. Magn. Reson. Spectrosc.* **2011**, 73, 63–82.
- [46] D. L. Bryce, C. M. Widdifield, R. P. Chapman, R. J. Attrell, *NMR of Quadrupolar Nuclei in Solid Materials* (Eds.: R. E. Wasylshen, S. E. Ashbrook, S. Wimperis), Wiley, Chichester (UK), **2012**, Chapter 19, pp. 321–348.
- [47] F. A. Perras, D. L. Bryce, *Angew. Chem.* **2012**, 124, 4303–4306; *Angew. Chem. Int. Ed.* **2012**, 51, 4227–4230.
- [48] R. J. Attrell, C. M. Widdifield, I. Korobkov, D. L. Bryce, *Cryst. Growth Des.* **2012**, 12, 1641–1653.
- [49] L. A. O'Dell, R. W. Schurko, *J. Am. Chem. Soc.* **2009**, 131, 6658–6659.
- [50] L. A. O'Dell, C. I. Ratcliffe, *Chem. Commun.* **2010**, 46, 6774–6776.
- [51] S. Cavadini, *Prog. Nucl. Magn. Reson. Spectrosc.* **2010**, 56, 46–77.
- [52] L. A. O'Dell, *Prog. Nucl. Magn. Reson. Spectrosc.* **2011**, 59, 295–318.
- [53] C. J. Pickard, F. Mauri, *Phys. Rev. B* **2001**, 63, 245101.
- [54] F. Mauri, N. Vast, C. J. Pickard, *Phys. Rev. Lett.* **2001**, 87, 085506.
- [55] M. D. Segall, P. J. D. Lindan, M. J. Probert, C. J. Pickard, P. J. Hasnip, S. J. Clark, M. C. Payne, *J. Phys. Condens. Matter* **2002**, 14, 2717–2744.
- [56] S. J. Clark, M. D. Segall, C. J. Pickard, P. J. Hasnip, M. I. J. Probert, K. Refson, M. C. Payne, *Z. Kristallogr.* **2005**, 220, 567–570.
- [57] C. Bonhomme, C. Gervais, F. Babonneau, C. Coelho, F. Pourpoint, T. Azais, S. E. Ashbrook, J. M. Griffin, J. R. Yates, F. Mauri, C. J. Pickard, *Chem. Rev.* **2012**, 112, 5733–5779.
- [58] E. van Lenthe, E. J. Baerends, J. G. Snijders, *J. Chem. Phys.* **1993**, 99, 4597–4610.
- [59] E. van Lenthe, E. J. Baerends, J. G. Snijders, *J. Chem. Phys.* **1994**, 101, 9783–9792.
- [60] E. van Lenthe, A. Ehlers, E. J. Baerends, *J. Chem. Phys.* **1999**, 110, 8943–8953.
- [61] E. van Lenthe, R. van Leeuwen, E. J. Baerends, J. G. Snijders, *Int. J. Quantum Chem.* **1996**, 57, 281–293.
- [62] A. Abate, M. Brischetto, G. Cavallo, M. Lahtinen, P. Metrangolo, T. Pilati, S. Radice, G. Resnati, K. Rissanen, G. Terraneo, *Chem. Commun.* **2010**, 46, 2724–2726.
- [63] a) M. T. Messina, P. Metrangolo, W. Panzeri, E. Ragg, G. Resnati, *Tetrahedron Lett.* **1998**, 39, 9069–9072; b) J. Viger-Gravel, S. Lelerc, I. Korobkov, D. L. Bryce, *CrystEngComm* **2013**, 15, 3168–3177.
- [64] C. M. Widdifield, D. L. Bryce, *J. Phys. Chem. A* **2010**, 114, 10810–10823.
- [65] B. Ellman, *J. Chem. Phys.* **2006**, 125, 074702.
- [66] R. Boese, T. Miebach, CCDC ID code: ZZZPRO05.
- [67] A. Hinchliffe, R. W. Munn, R. G. Pritchard, C. J. Spicer, *J. Mol. Struct.* **1985**, 130, 93–96.
- [68] C. M. Widdifield, R. W. Schurko, *Concepts Magn. Reson. A* **2009**, 34, 91–123.
- [69] M. Bak, J. T. Rasmussen, N. C. Nielsen, *J. Magn. Reson.* **2000**, 147, 296–330.
- [70] B. Alonso, D. Massiot, P. Florian, H. H. Paradies, P. Gaveau, T. Mineva, *J. Phys. Chem. B* **2009**, 113, 11906–11920.
- [71] J. Viger-Gravel, I. Korobkov, D. L. Bryce, *Cryst. Growth Des.* **2011**, 11, 4984–4995.
- [72] E. A. C. Lucken, *Nuclear Quadrupole Coupling Constants*, Academic, London, **1969**.
- [73] G. K. Semin, T. A. Babushkina, S. P. Khrlakyan, E. Y. Pervova, V. V. Shokina, I. L. Knunyants, *Theor. Expt. Chem.* **1971**, 4, 179–181.
- [74] C. I. Wynter, J. Hill, W. Bledsoe, G. K. Shenoy, S. L. Ruby, *J. Chem. Phys.* **1969**, 50, 3872–3874.
- [75] K. J. D. MacKenzie, M. E. Smith, *Multinuclear Solid-State NMR of Inorganic Materials*, Pergamon, Amsterdam, **2002**.
- [76] M. G. Sarwar, B. Dragisic, L. J. Salsberg, C. Gouliaras, M. S. Taylor, *J. Am. Chem. Soc.* **2010**, 132, 1646–1653.
- [77] A. L. Webber, B. Elena, J. M. Griffin, J. R. Yates, T. N. Pham, F. Mauri, C. J. Pickard, A. M. Gil, R. Stein, A. Lesage, L. Emsley, S. P. Brown, *Phys. Chem. Chem. Phys.* **2010**, 12, 6970–6983.
- [78] P. Metrangolo, W. Panzeri, F. Recupero, G. Resnati, *J. Fluorine Chem.* **2002**, 114, 27–33.
- [79] V. R. Thalladi, H.-C. Weiss, D. Bläser, R. Boese, A. Nangia, G. R. Desiraju, *J. Am. Chem. Soc.* **1998**, 120, 8702–8710.
- [80] G. Metz, X. Wu, S. O. Smith, *J. Magn. Reson. Ser. A* **1994**, 110, 219–227.
- [81] A. E. Bennett, C. M. Rienstra, M. Auger, K. V. Lakshmi, R. G. Griffin, *J. Chem. Phys.* **1995**, 103, 6951–6958.
- [82] B. M. Fung, A. K. Khitrin, K. Ermolaev, *J. Magn. Reson.* **2000**, 142, 97–101.
- [83] E. L. Hahn, *Phys. Rev.* **1950**, 80, 580–594.
- [84] S. Hayashi, K. Hayamizu, *Bull. Chem. Soc. Jpn.* **1991**, 64, 685–687.
- [85] S. Hayashi, K. Hayamizu, *Bull. Chem. Soc. Jpn.* **1991**, 64, 688–690.
- [86] I. Solomon, *Phys. Rev.* **1958**, 110, 61–65.
- [87] D. Massiot, I. Farnan, N. Gautier, D. Trumeau, A. Trokner, J. P. Coutures, *Solid State Nucl. Magn. Reson.* **1995**, 4, 241–248.
- [88] A. Medek, V. Frydman, L. Frydman, *J. Phys. Chem. A* **1999**, 103, 4830–4835.
- [89] R. W. Schurko, S. Wi, L. Frydman, *J. Phys. Chem. A* **2002**, 106, 51–62.
- [90] C. M. Widdifield, D. L. Bryce, *J. Phys. Chem. A* **2010**, 114, 2102–2116.
- [91] C. M. Widdifield, A. D. Bain, D. L. Bryce, *Phys. Chem. Chem. Phys.* **2011**, 13, 12413–12420.
- [92] L. A. O'Dell, R. W. Schurko, K. J. Harris, J. Autschbach, C. I. Ratcliffe, *J. Am. Chem. Soc.* **2011**, 133, 527–546.
- [93] M. Witanowski, L. Stefaniak, G. A. Webb, *Annu. Rep. Nucl. Magn. Reson. Spectrosc. B* **1982**, 11, 1–486.
- [94] J. S. Frye, G. E. Maciel, *J. Magn. Reson.* **1982**, 48, 125–131.
- [95] K. Eichele, R. E. Wasylshen, *WSolids1: Solid-State NMR Spectrum Simulation Package*, Dalhousie University, Halifax, **2009**.
- [96] J. R. Yates, C. J. Pickard, F. Mauri, *Phys. Rev. B* **2007**, 76, 024401.
- [97] M. Profeta, F. Mauri, C. J. Pickard, *J. Am. Chem. Soc.* **2003**, 125, 541–548.
- [98] D. Vanderbilt, *Phys. Rev. B* **1990**, 41, 7892–7895.
- [99] J. P. Perdew, K. Burke, M. Ernzerhof, *Phys. Rev. Lett.* **1996**, 77, 3865–3868.
- [100] J. P. Perdew, K. Burke, M. Ernzerhof, *Phys. Rev. Lett.* **1997**, 78, 1396.
- [101] R. P. Chapman, J. R. Hiscock, P. A. Gale, D. L. Bryce, *Can. J. Chem.* **2011**, 89, 822–834.
- [102] G. te Velde, F. M. Bickelhaupt, E. J. Baerends, C. F. Guerra, S. J. A. van Gisbergen, J. G. Snijders, T. Ziegler, *J. Comput. Chem.* **2001**, 22, 931–937.
- [103] C. Fonseca Guerra, J. G. Snijders, G. te Velde, E. J. Baerends, *Theor. Chem. Acc.* **1998**, 99, 391–403.
- [104] SCM, Theoretical Chemistry, Vrije Universiteit, Amsterdam, The Netherlands, ADF v. 2012.01 <http://www.scm.com>.
- [105] E. van Lenthe, J. G. Snijders, E. J. Baerends, *J. Chem. Phys.* **1996**, 105, 6505–6516.
- [106] S. H. Vosko, L. Wilk, M. Nusair, *Can. J. Phys.* **1980**, 58, 1200–1211.
- [107] Y. Zhang, W. Yang, *Phys. Rev. Lett.* **1998**, 80, 890–890.

Received: March 1, 2013

Revised: June 10, 2013

Published online: July 26, 2013